Tendon-Driven Notched Needle for Robot-Assisted Prostate Interventions

A THESIS SUBMITTED TO THE GRADUATE DIVISION OF THE
UNIVERSITY OF HAWAIʻI AT MĀNOA IN PARTIAL FULFILLMENT
OF THE REQUIREMENTS FOR THE DEGREE OF

MASTER OF SCIENCE

IN

MECHANICAL ENGINEERING

DECEMBER 2022

By
Zolboo Batsaikhan

Thesis Committee:

Bardia Konh, Chairperson
Peter Berkelman
Scott Miller

Keywords: notched needle, active needle, robotic needle insertion, prostate cancer

ACKNOWLEDGEMENTS

First and foremost, I would like to thank my advisor, Dr. Bardia Konh, who welcomed me to the Advanced Materials and Medical Instruments (AMMI) lab and supported my research despite the many challenges that were encountered. I would also like to thank my colleagues, Blayton Padasdao, Mahsa Rabiei, and Samuel Lafreniere, members of the AMMI lab, who helped and supported me throughout my studies. I also owe a huge thank you to Dr. Philip von Doetinchem for the teaching assistant position and the invaluable experience I gained at the Physics lab. Lastly, I would like to thank my MS thesis committee, Drs. Peter Berkelman and Scott Miller for their help and insight.

ABSTRACT

Needle insertion techniques have shown a high potential to improve the outcome of several diagnostic and therapeutic minimally invasive procedures. One example is high-dose-rate (HDR) brachytherapy (BT), a radiation therapy, in which radioactive sources are placed at cancerous tissue using needles. HDR BT offers dose conformality and sparing of clinical structures, lower operator dependency, and fewer acute irritative symptoms. However, HDR BT is limited for patients with pubic arch interference (PAI), where the transperineal path to the prostate is blocked. Active and flexible needles that can maneuver in the desired path could be a solution. Another example is targeted prostate biopsy, an effective image-guided technique that detects significant cancer via fewer cores and a lower number of unnecessary biopsies compared to traditional systematic (12-core) biopsy.

This work presents two tendon-driven notched needle designs: (i) a unidirectional needle design for HDR BT patients with PAI and (ii) a bidirectional needle design for targeted prostate biopsy interventions. Compliant flexure sections of the notched needle were fabricated on a nitinol tube that enables unidirectional and bidirectional bending via actuation of internal tendon(s). Experimental evaluations with the unidirectional needle design showed the feasibility of the needle moving around the pubic arch for placement at hard-to-reach target positions. For the bidirectional needle design, kinematic and static models of the compliant flexure section have been presented and validated with experiments. The capability of the notched needle to bend, reach targeted positions inside a phantom tissue, and extract a biopsy sample is shown.

Table of Contents

LIST OF TABLES

LIST OF FIGURES

LIST OF ABBREVIATIONS

HDR BT	High-Dose-Rate Brachytherapy
LDR BT	Low-Dose-Rate Brachytherapy
PAI	Pubic Arch Interference
PSA	Prostate-Specific Antigens
TRUS	Transrectal Ultrasound
MRI	Magnetic Resonance Imaging
CT	Computed Tomography
BT	Brachytherapy
FBG	Fiber Bragg Grating
EM tracker	Electromagnetic Tracker
SMA	Shape Memory Alloy
SME	Shape Memory Effect
Ni-Ti	Nickel-Titanium
EDM	Electrical Discharge Machining
PVC	Polyvinylchloride
ROM	Rang of Motion
US	Ultrasound

LIST OF SYMBOLS

t	Cut width
d	Cut depth
d_n	Distance between notches
d_h	Round hole diameter
$\bar{y}$	Distance moved from the center of the tube
r_o	Outer radii
r_i	Inner radii
θ_i	Bending angle for each notch
h	Height of the neutral axis
F	Tendon tension
T	Torque
d_m	Mean diameter of single notch
l	Tendon displacement
f	Coefficient of friction
α	Notch angle
θ_{total}	Bending angle of a flexure section
N	Number of notches
θ_{notch}	Bending angle of a single notch
U	Total internal energy
M_r	Moment at the cross section
E	Young modulus
F_1	Force applied on each notch
w	Width of section
I	Moment of area with respect to y-axis
M	Moment applied to the section

Chapter 1. INTRODUCTION

Needle-based interventions have been widely used for prostate cancer diagnosis and treatments. Despite of the improvements in needle steering, the success of these procedures has hindered by the low accuracy in needle placement at target locations. This section describes needle-based interventions in prostate cancer diagnoses and treatment, importance of targeting accuracy, and provides a literature review on previous needle designs and needle steering methods.

1.1. Needle-based interventions in prostate cancer

Prostate cancer is the most common cancer among men with an estimated 268,490 in the United States and 1,414,259 new cases worldwide in 2022 [1]. Prostate cancer usually diagnosed in older men when tumorous cells start growing in prostate gland. Needle-based interventions are commonly used to diagnose and treat prostate cancer through various proceedings known as prostate biopsy and brachytherapy. In recent years, surgical instrument development has been at the forefront of research investigations to help physicians perform the surgical procedures more accurately. New surgical needles are being developed to aid surgeons in precise positioning of the needle at the target location.

1.1.1. Needle-based prostate cancer diagnoses

Prostate cancer could have no signs or symptoms at its early stage as it grows prolonged where it may not cause serious harm. However, early detection of prostate cancer is essential to reduce mortality rates and metastasis [2]. To diagnose prostate cancer, clinicians commonly perform a screening for prostate-specific antigens (PSA) in conjunction with performing a digital rectal exam. If the examination results are abnormal, a prostate biopsy or treatment is administered depending on the PSA levels. A study of about 19,000 males concluded that even though some patients had less than "normal" range of PSA levels, they were later correctly diagnosed with prostate cancer through a biopsy [3].

Image-guided biopsy has been a popular procedure for diagnosing prostate cancer for decades. However, poor needle placement and tumor visualization have always been among the problems resulting in clinicians classifying the tumor as benign when it was malignant (i.e., false negative). The prostate cancer and imaging technology workshop by the National Cancer Institute [2] reported diagnostic accuracy as one of four significant challenges in prostate cancer treatment and management. A typical diagnosis method for prostate cancer is a core needle biopsy. Unfortunately, transrectal ultrasound (TRUS) guided biopsies have resulted in a poor cancer detection rate of 20-30% [2]. In addition, due to the inherent heterogeneity of prostate cancer (~85% of prostate cancer being multifocal in origin [3]), systematic biopsy methods (6–12 spatially distributed prostate core biopsies under TRUS guidance) might also not provide accurate information on location, size, extent, and grade of the disease. Even systematic sampling done with TRUS guidance often resulted in the underdiagnosis of prostate cancer.

Current studies [4,5] have shown that targeted biopsy results in the detection of significant cancers with fewer cores, thereby reducing unnecessary biopsies. The success of the targeted

biopsy depends on (i) Magnetic Resonance Imaging (MRI) detection of significant cancer and (ii) accurate targeting of the biopsy [6]. Previous studies have emphasized the former, while the impact of targeting accuracy on overall performance has been ignored [6]. Enhancing targeting accuracy demands better conveying the target location to the biopsy operator [6]. The experience also impacts targeting accuracy, meaning that more skilled operators have better targeting results [7].

1.1.2. Needle-based prostate cancer treatment

Existing treatment options for prostate cancer include brachytherapy, external beam radiation therapy, radical prostatectomy, cryotherapy, and hormonal therapy. Of these, brachytherapy, an outpatient procedure where local radiation is used to irradiate cancer inside the prostate, is one of the well-known modalities [8,9].

Patients with early-stage prostate cancer are generally chosen for LDR BT [10]. Currently, a 'stepper' instrument allows calibrated linear translation of a transrectal ultrasound (TRUS) through the rectum, while a set of needles is used for percutaneous implantation of radioactive seeds [11]. The physician uses the needle to deposit about 50-100 seeds in the prostate. Several approaches, such as computed tomography (CT) and MRI, are utilized for post-implant dosimetry [12]. Since a high radiation dose with an intense fall-off is delivered to the prostate gland, precise placement of the seeds is required to ensure an effective treatment [10,13]. Limited needle actuation near the needle's entry point into the tissue, movement of the target location during needle insertion [14,15] along with the distribution of 70% of the tumor foci at the peripheral zone of the prostate [16] result in additional complications for precise seed placements and desired dose distribution.

During HDR BT, 18- or 17-gauge needles (catheters) are carefully inserted inside the prostate through the perineum. This process is done manually by a doctor under TRUS guidance.

Rigid needles and standard templates limit the needle's maneuverability, and thereby, puncture of organs at risk, such as the penile bulb and connected vasculature, is often inescapable. After needle placements, a CT scan provides a 3D image of the prostate, catheters and the critical organs like the bladder and rectum. With the help of CT images, it radiates only to target areas inside the prostate, not the healthy part of the organ. An automatic device, called a remote afterloader, is then utilized to insert a radiation source, called Iridium, through several channels connected to the implanted catheters. The radiation source is welded on the end of a wire, allowing removal after the procedure. The device is programmed to provide different radiation doses at different positions in the prostate.

Most studies have reported similar outcomes using either HDR or LDR BT [12]. However, HDR BT eliminates the limitations in seed loss or displacement in LDR BT that can lead to suboptimal dosimetry, including cold areas within the prostate and higher doses than intended for the urethra, rectum, and bladder [17]. The benefits of HDR BT include adequate dose conformality and sparing of clinical structures, lower operator dependence, and fewer acute irritative symptoms. Another study argued that the declining trend in using BT [18–20] is due to a lack of skilled radiation oncologists to perform high-quality BT implants.

Existing BT procedures can result in side effects such as edema in tissue, incontinence, and impotence. Due to excessive radiation and needle penetration into sensitive organs such as the urethra, bladder, rectum, penile bulb, cavernous veins, and neuro-vascular bundles cause the side effects. Furthermore, HDR BT is limited in patients whose pubic arch obstructs the transperineal path to the prostate, thereby interfering with needle placement [21]. Nickers et al. [22] found the procedure is practical only for 24 out of the 40 patients studied due to pelvic bone arch interference. Substantial pubic arch interference (PAI), which is more likely to occur in patients with a large

prostate, causes it challenging to achieve adequate source placement in the anterior and lateral portions of the prostate [23]. Even a narrow pubic arch may prevent proper implantation in a small prostate gland [23]. Available strategies to overcome this problem, including oblique catheter insertion and pelvic rotation [24,25], are not optimal solution.

1.2. Importance of targeting accuracy

The success of prostate biopsy and brachytherapy (like many other needle-based interventions) relies on the accurate placement of the needle tip at the cancerous tissue to take a sample or plant the radioactive seeds, respectively. While misplacing biopsy needles in a target location causes misdiagnosing cancer, placing the needles or radioactive seeds close to the urethra or rectum in HDR BT and LDR BT could also cause unnecessary dose delivery and damage these healthy organs.

In needle-based interventions , the target moves due to physiological processes such as breathing, intervening anatomy, needle bending, poor needle visualization, and limited imaging possibilities are the factors causing it challenging to reach the target [26]. Due to tissue inhomogeneity, the needle can also deviate from its desired path [27]. In the case of deviation from the desired path, the surgeons remove and reinsert the needle back into the tissue. Steering the needle can alleviate this concern by precisely placing needles at desired locations.

1.3. Literature review on steerable needles

It was reported [28] that a mean maximal error of 2.7mm in needle placement is acceptable in targeting lesions in needle-based interventions. Several improvements have been made in recent years in medical imaging and interventional delivery systems, but without enhancing the needle design. The design of most clinical needles remained the same.

Most surgical needles available in the clinic offer a straight path starting at the entrance point of the initial puncture towards the target. These needles have limitations on the accessibility to the targets and the possibility of puncturing other sensitive organs on the way to the target. These punctures are detrimental to the patients and may have long-lasting severe side effects.

Consequently, steering needles could increase the efficacy of needle-based interventions in cancer cases. By enhancing the steerability of the needles, previously unreachable target areas could be reached without any additional damage or rupture in the tissues or other organs along the way to the target. Flexible needles are introduced to enable needle insertion in a curved path and potentially decrease the targeting error. Many researchers have developed different methods to make flexible needles to steer them inside the soft tissue.

Several needle steering approaches [29–34] have been reported to guide the needle inside the tissue. The steering approaches [35,36] can be grouped into four categories: (i) tissue manipulation, (ii) lateral needle manipulation, (iii) tip-based steering, and (iv) “shaft-based” steering.

Passive needles have been proposed for diagnosis or therapeutic purposes [37–40]. Bevel-tip [41], pre-curved [42,43], kinked needles [44], flexure-based needles [44], and concentric pre-curved tubes [45,46] are among the most effective needle steering methods. However, trajectory planning with passive needles is complicated and sometimes inaccurate [47,48]. With passive

needles, the deflection is realized by nonhomogeneous viscoelastic interactions between tissue and needle. Passive needles with a predefined shape steer in a 2D plane with a constant radius, thereby requiring an axial rotation for 3D placement. Rotation of the needle while advancing through the tissue may increase the risk of tissue damage [41]. Concentric tubes [45] offer a wider reachability region close to their current state in an insertion task, although there is still a need for axial movement to reach the target. In addition, steerable bevel tip needles are subject to nonholonomic constraints [49]. The needle is considered an under-actuated system that is not locally controllable [50]. This means that any state close to the needle's current state is not reachable in an arbitrarily short amount of time by paths close to its current state [51]. Active needles, contrastingly, provide a source of actuation and, thereby, more control over the system.

When accurately controlled, active needles [36,52–54] can compensate for needle placement errors caused by unpredicted factors during insertion, such as tissue deformation and unstable puncture force. Examples of active tendon-driven needles can be found in [55–59]. Some active needle designs demand a highly flexible needle tube while bending by a tendon actuation. Some research groups [54–57,60] have used different forms of cutout patterns on a superelastic Nitinol tube to achieve higher flexibility. Shape memory alloy wires have also been used to actively bend the needles in the works of Ryu and coauthors [61,62], Chitalia et al. [63,64] and, Ayvali et al.[52].

Table 1 shows the comparison of the state-of-the-art steerable needles used in research. Passive needles [65,66] with 1.4mm and 1.2mm outer diameter realizes maximum tip deflection of 20mm and 17mm, respectively. This is not sufficient for reaching targets inside the prostate with fewer insertions and targets that are blocked by pubic arch interference which will be discussed later. Active needles [67–69] can achieve sufficient degree of deflection for prostate

interventions, however, these needles cannot pass through biopsy tray and radioactive seeds for LDR BT due to its smaller shaft diameter.

Table 1. Comparison between state-of-the-art steerable needles used in research.

Needle category	Needle diameter	Deflection	Medical Application	Prostate Interventions	Reference
Passive	1.4mm	20mm	Prostate BT	Applicable	Vries [65]
Passive	1.2mm	N/A	Biopsy	Applicable	Moreira [66]
Passive	0.83mm	17mm	Lung surgery	N/A	Shahriari [67]
Active	2.0mm	68.4 degrees	Catheter behavior	N/A	Sikorski [65]
Active	6.0mm	15.9 degrees	Prostate BT	Applicable	Blayton [70]
Active	1.8mm	12.4 degrees	Biopsy	Applicable	Blayton [69]
Active	0.8mm	60 degrees	Biological tissue	N/A	Troy [68]
Active	2.0mm	30.92 degrees	Prostate BT	Applicable	Chapter 2
Active	2.0mm	31.67 degrees	Biopsy	Applicable	Chapter 3

1.4. Needle steerability and sensing

Needle trajectory planning is a challenging task due to tissue's viscoelastic properties and target movement during a needle insertion procedure. In addition, with the optimum steering strategies and determination of insertion points, motion planning can be more efficacious in improving the needle tip placement at the target [71]. Moreover, needle steering can be done under a real-time fluoroscopic guidance where a closed-loop control and steering is demonstrated with the error level below 0.5mm for 40mm trajectory length [72].

For needle steering in 3D, a feedback control along with helical paths may be presented to correct perturbations with varying the helix radius [73]. In this method, needle deflection is collected by an imaging feedback system which improves the needle trajectory to get as close to the planned target as possible with controlling of the radius and heading of the helix.

1.5. Shape memory alloy – super elastic property

Shape Memory Alloys (SMAs) [74–78] are a group of materials used in various types of applications in different fields. The SMAs are known for their "Superelasticity" to recover a large deformation caused by loading conditions via temperature changes. SMAs can also produce a high rate of actuation energy density, known as the Shape Memory Effect (SME). These special characterizations of SMAs make them suitable for sensing, actuation, absorption, and vibration damping applications. Actuation of SMAs refers to their SME behavior, which could be shown as a cyclic hysteresis diagram representing phase transformation between Austenite at high and Martensite at low temperatures. SMAs' characteristics and thermomechanical behavior, such as SME, superelasticity, and biocompatibility, in addition to corrosion resistance, make SMAs suitable for biomedical applications. Mainly, Nickel-Titanium (Ni-Ti), known as Nitinol [79] (made of two elements of Nickel at ~50% and Titanium at ~50%), is a part of SMAs family used in some minimally invasive medical devices [80]. Some of the most popular medical and biomedical applications of SMAs are orthopedic, cardiovascular, dental applications, and surgical and clinical instruments [81,82]. Due to its biocompatibility and corrosion resistance, nitinol is used in many biomedical applications. Considering the superelastic characteristics, nitinol stents have been used in order to treat artery disease where blood flow to the heart is reduced. The Nitinol stents expand to a suitable diameter with sufficient force to open the vessel lumen and restore blood flow.

In this work, due to its superelastic characteristics and shape memory effect, nitinol tube as well as SMA wire were used as a needle shaft and actuator cable, respectively. The nitinol tubes make the needles bendable in various directions, while the shape memory effect offers a reliable actuation to apply bending forces to the needles.

1.6. Contribution

This thesis aims to develop active steerable needles for surgical procedures such as HDR prostate BT and targeted prostate biopsy. The active steerable needles are capable of deflecting its shaft into two directions at a high degree to reach targets inside the tissue. It is organized to demonstrate a robotically controlled needle bending in air and show the ability of bending in tissue-mimicking phantom using different proposed steerable needles. EM trackers were utilized to sense the needle pose for determining bending angle in air and ultrasound system was used to determine the needle tip in the phantom tissue. This will be discussed more in detail in the next chapters.

Chapter 2. Uni-Directional Steerable Active Needle for HDR BT – Design, Control and Performance Evaluation

Section 2.1 explains the needle bending requirement of HDR BT for patients with Pubic Arch Interference (PAI). Section 2.2 introduces a novel design concept of a tendon-driven notched needle with a capability of bending in a one direction. Section 2.3 describes the needle flexure section fabrication method used in this work. Section 2.4 discusses the modeling and bending calculation of the flexure section. Section 2.5 describes the insulation method of the flexure section. A robotic actuation system designed to actuate the flexure section of the needle is discussed in section 2.6. Finally, the results section investigates the performance of the needle bending in air and phantom tissue.

2.1. Needle bending requirement for patient with PAI

Traditional prostate brachytherapy procedures for patients with larger prostate are challenging due to some parts of the prostate being blocked by the pubic arch. This causes PAI and it has been reported in 10% of patients with early stages of prostate cancer, to whom HDR BT is not a treatment option [83].

Bending the needles makes it possible to reach the target areas that are not reachable by straight needles and to avoid puncturing the urethra during needle placements. Figure 1 shows the coronal view of the workspace in BT with needles inserted from the perineum into the prostate. As shown in the figure, some target areas are not reachable with straight needles. To estimate the amount of needle bending required to reach the target positions, the interference can be estimated at 10mm between the pubic arch and the prostate gland. The dimensions of the prostate (44mm in width, 31mm in height, and 38mm in length) were used based on the average prostate size for male patients between the ages of 40 and 50 [84]. It was estimated that about 28 degrees of angular deflection are sufficient for the needle to reach the target (marked in the figure at a depth of 140mm).

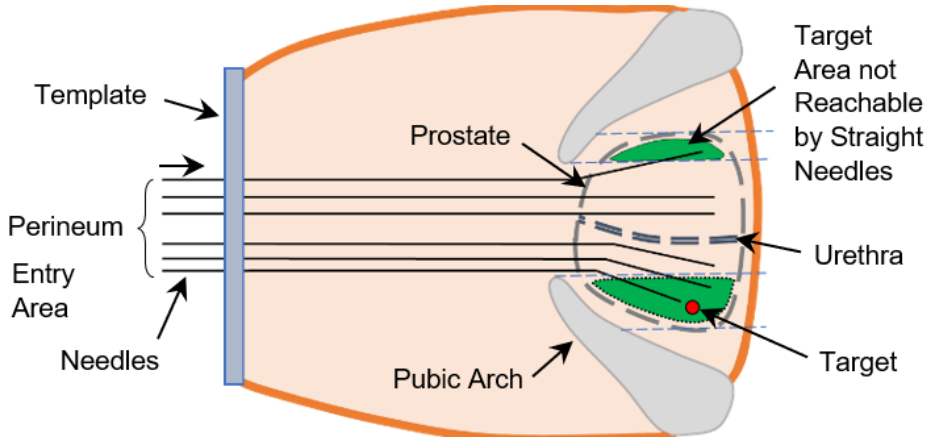

Figure 1. Coronal view of the workspace for prostate BT. Needles are inserted from the perineum into the prostate.

2.2. Design concept of the uni-directional notched needle

Recent studies have shown that needle flexibility and bendability can be potentially improved by making a pattern of notches on the needle. However, current needles do not have the ability to bend at high degrees at a short distance due to their design constraints. Reaching higher degrees of needle bending inside the prostate while ensuring the safety of the procedure, a notched needle with a capability to bend in uni direction was designed. This design was selected for the purpose of HDR and LDR BT. For these procedures, radioactive seeds or catheters are delivered through the needle tube. One of the most important needle design requirements was the inner diameter of the needle tube that should be able to pass seeds or catheters when it is in the bent position. Thus, the following design was selected to maximize the inner diameter of the tube as well as the bending angle of the flexible section.

Figure 2a shows a 2D drawing of the flexible section of a uni-directional notched needle. Figure 2b shows each notch's dimensions that need to be carved on the needle tube for improved flexibility. A super elastic nitinol tube (Johnson Matthey, London, UK) with an outer and inner diameter of 1.80 and 1.55mm, respectively, and a tube thickness of 0.125mm was used as a needle shaft. A series of seven notches were made on the needle tube to create a compliant section for additional flexibility. Even though nitinol is a highly flexible material, plastic deformation occurs when the bending angle at each notch passes its limit. The width and depth of the notches play an important role in flexure section design. The following design was chosen due to its increased flexibility while avoiding plastic deformation. Round-shaped cuts were made on the side of the needle to enable more flexibility. Thin notches that connect the round-shaped cuts physically limit their movement to avoid plastic deformation.

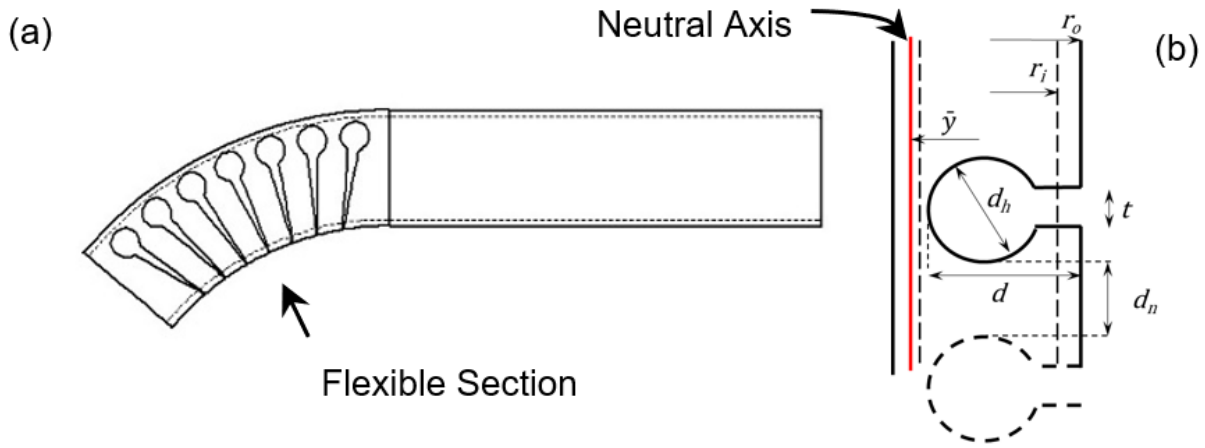

Figure 2. (a) Design of the flexible section of the needle, (b) notch parameters

The dimensions of the seven notches are listed in **Error! Reference source not found.**. The average cut width (t), depth (d), and distance between the notches (dn) were 0.14±0.05, 1.57±0.03, and 0.36±0.06mm, respectively. These values were selected to achieve required needle bending to avoid PAI. The average diameter of the round notches was 0.59±0.03mm. The overall length of the flexible section was 5.86mm. Two small holes (diameter of about 0.25mm) were made close to the distal end of the needle for a tendon (a nitinol wire of 0.13mm diameter) to get attached. The tendon was looped in and out of the holes to secure its place. The tension of the tendon assures bending in the direction of the notches.

Table 2. Dimensions of the seven notches carved on the needle tube. Units are in mm.

Notch	1	2	3	4	5	6	7
Cut Width (t)	0.12	0.15	0.10	0.09	0.13	0.12	0.25
Round Hole Diameter (d_h)	0.61	0.61	0.61	0.60	0.60	0.55	0.56
Cut Depth (d)	1.60	1.59	1.58	1.53	1.52	1.56	1.60
Distance between the Notches (d_n)	N.A.	0.29	0.45	0.40	0.30	0.39	0.34

2.3. Fabrication process

Previous studies have shown [56,59] that other manufacturing methods, such as electrical discharge machining (EDM) or femtosecond laser, can produce round and smooth corners to alleviate stress concentrations. In this work, however, the needle was fabricated in the lab using a traditional machining process. A custom needle-making set-up (shown in Figure 3) was designed to make the notches, including a 3D printed needle fixture, micro-meter 3DOF screw gauge, Dremel, Ultra-thin cut-off disks, camera, and water spray. The 3D printed needle fixture (shown in Figure 3) was designed to hold the needle stable while allowing the Dremel to make notches. The fixture was designed with a needle-sized hole along its body to restrict the needle shaft movement during the machining process. A slot with length of 1 cm at the end of the needle fixture was created to monitor the machining process. An iPhone 12 camera was used to help facilitate the fabrication of the cuts. The needle fixture was fixed to the micrometer screw gauge to precisely set the desired cut depth and spacing between the notches. The property of the nitinol is affected by the temperature. Therefore, water was applied throughout the cutting process to allow an effective heat transfer and to avoid high temperatures. The notches were made using thin cut-off disks with a thickness of 0.5mm and 0.127mm (Gesswein & Co., Inc., Bridgeport, Connecticut). First, seven circular-shaped cuts were made on the side of the tube using a 0.5mm disk. Second, cuts with the same size and distance were made 180 degrees apart from the cuts previously made. Then, the thin notches were made to connect each circular cuts using a 0.127mm disk.

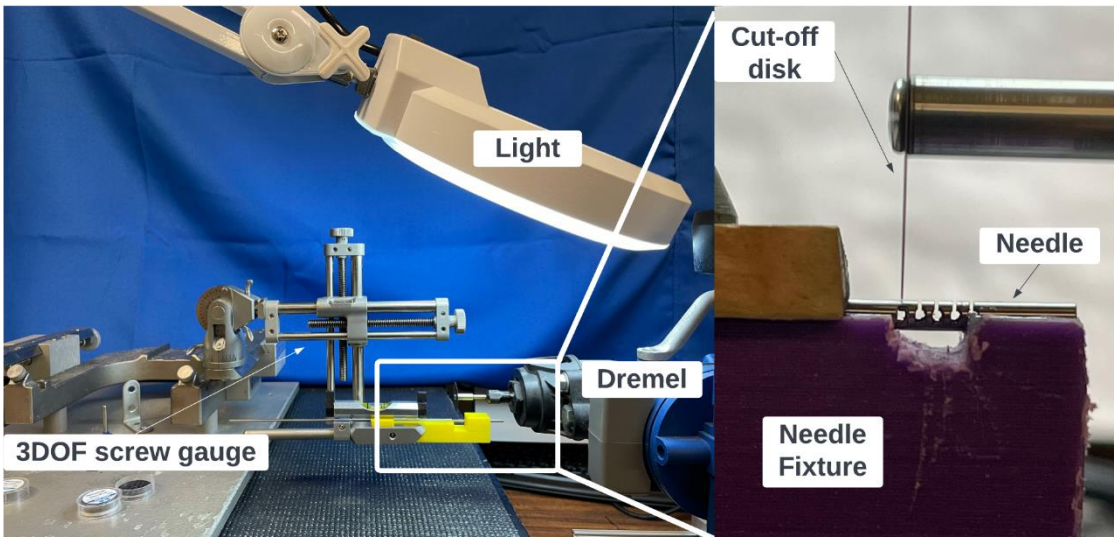

Figure 3. Custom needle-making set-up

2.4. Modeling and bending calculation

Equations 1 to 4 explain methods to estimate the bending angle for the needle's flexible section. For the notched needle tube presented in Section 2.2, the neutral bending axis can be calculated using the following equation [85]:

$$\bar{y} = \frac{4(r_o{}^3 \, sin^3(\phi_o) - r_i{}^3 \, sin^3(\phi_i))}{3\left(r_o{}^2(2\phi_o - sin\,2\,\phi_o) - r_i{}^2(2\phi_i - sin\,2\,\phi_i)\right)} \quad (1)$$

where $\bar{y}$ is the distance moved from the center of the tube, r_o and r_i are the outer and inner radii of the tube, respectively, and ϕ_o and ϕ_i are found by the following equations:

$$\phi_o = arccos(\frac{d - r_o}{r_o}) \quad (2)$$

$$\phi_i = arccos(\frac{d - r_o}{r_i}) \quad (3)$$

where *d* is the notch depth. The bending angle for each notch can be estimated as:

$$\theta_i = \frac{h}{r_o + \bar{y}} \quad (4)$$

where *h* is the height of the neutral axis for each, which in this work is equal to the height of the cut width (*t*). for the notch dimensions shown in Figure 2b, an angular deflection of 4.58 degrees is estimated on each notch. Assuming that the total deflection is distributed equally along all the notches, the bending angle of the whole flexible section can be found by multiplying the bending angle of each notch by the number of notches. Thereby, an overall bending angle is about 32.06 degrees for the notched needle introduced in this work.

2.5. Heat shrink cover

The flexible section of the needle was covered with a biocompatible ultrathin (wall thickness of 76μm) medical-grade heat shrink tubing made from Polyolefin (Cobalt Polymers, Cloverdale, CA) to prevent rupture of the tissue at the sharp edges of the notches. The heat shrink cover provides insulation to prevent tissue from entering the needle tube. Figure 4a and b show the needle in straight and bent configurations. The heat shrink cover slightly increased the outer diameter of the needle to 1.876mm and the stiffness of the flexible section. The flexible joint of the needle was bent about four degrees when covered with heat shrink tubing. Insulation was tested by filling the needle tube with water while one end of the tube was covered. The procedure was observed for 30 minutes and no leakage was realized.

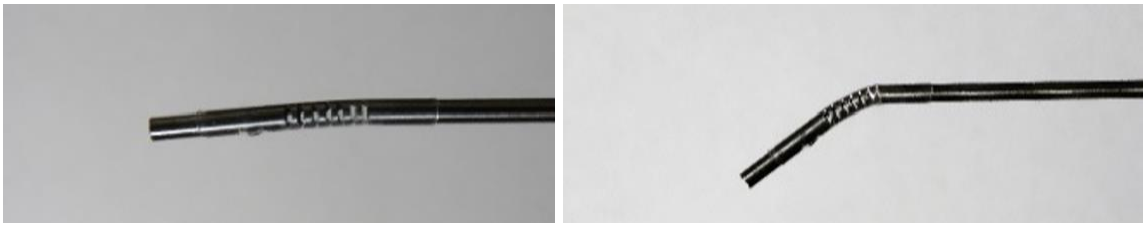

Figure 4. (a) Heat shrink cover, and (b) deflected shape of the needle.

2.6. Robotic needle actuation system

The tendon tension (*F*) that is required to realize a specific bending on the flexible section of the needle should be carefully estimated to design a functional actuation and control system. The following equation was used to calculate the amount of torque (*T*) required to pull the tendon and consequently bend the needle, similar to lowering down a load on a lead screw:

$$T = \frac{F d_m}{2}\left(\frac{l + \pi f d_m \sec\alpha}{\pi d_m - f l \sec\alpha}\right) \quad (5)$$

where d_m, *l, f, and* α are the mean diameter of a single notch, tendon displacement, coefficient of friction, and notch angle, respectively. It is estimated that a maximum of 22N of force (tendon tension) must be sufficient to bend the notched needle inside the tissue. With this amount of tension, an 8mm diameter lead screw, friction coefficient of 0.25 for threaded pairs of a steel and dry screw, and thread angle of zero for square threads, the maximum torque was estimated as 0.41Nm. Accordingly, a DC motor, gear, and a lead screw combination was selected and purchased from Maxon Group, Sachseln, Switzerland.

The combination consists of a 0.5W Maxon DC motor RE 8 Ø8 mm, Precious Metal Brushes) with an 8mm diameter lead screw drive (GP 8 S Ø8mm, Metric spindle, M3 x 0.5), and an encoder (MR, Type S, 100CPT). The Maxon motor was connected to a computer using a EPOS4 digital positioning controller and programmed using Maxon Group's software, EPOS Studio. The software communicates with Maxon Group's EPOS4 positioning controller to give the user control on the position, velocity, and acceleration profiles. In order to run under the safe conditions of the motor system at high incremental position value (600000inc or 3mm), an rpm of 10000 was chosen with a 500rpm/s acceleration and deceleration rate to form a trapezoidal profile. This allows the system to quickly reach the target position without overshooting.

Two holders were designed, and 3D printed to hold the motor and the lead screw (shown in Figure 5a). Holder 1, housing a nut on the lead screw, was mounted on a 50mm long linear rail guide (MGN9H) to translate rotational movement of the motor shaft to linear movement. Holder 2 was stationary, keeping the position of the motor. The holders are designed to ensure that all the movement occurs on the same plane. The free end of the tendon was fixed on Holder 1. The tendon is threaded through the midpoint of the holder to ensure colinear movement.

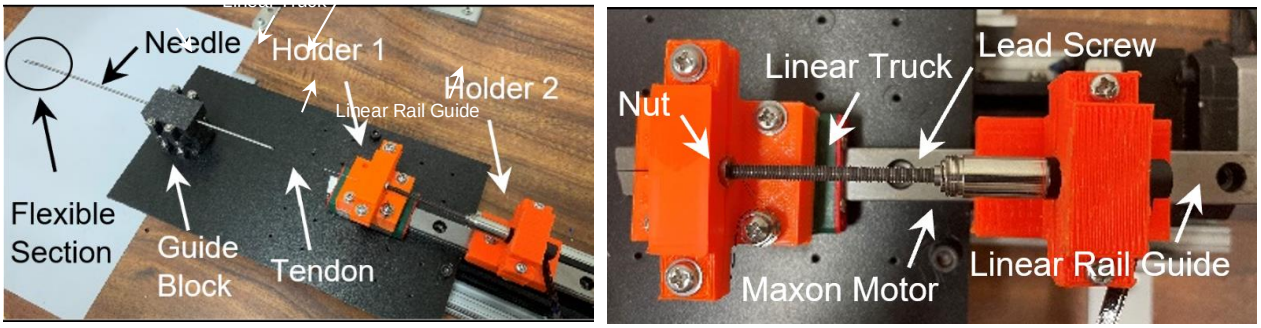

Figure 5. Actuation and control system to pull the tendon and bend the notched needle: (a) assembled on a linear stage for needle axial insertion, and (b) Maxon motor, gear box, and lead screw.

The Maxon motor, gear box, and lead screw (shown in Figure 5b) were mounted on a linear stage for needle insertion tests in a phantom tissue. The Maxon motor pulls the tendon axially to bend the needle. The motor is fixed to a linear motion guide rail with the lead screw nut being held in place on a movable platform along the rail. The needle is considered at the maximum bending position when the cable tendon is pulled 3mm in the axial direction due to the notches in the needle touching each other.

2.7. Results

2.7.1. Needle deflection in air

Figure 8 shows the angular bending of the needle realized by the tendon displacement in the air. The error bars were calculated to show the higher and lower values in five trials. A maximum bending angle of 30.92 degrees was demonstrated, comparable with the bending calculations of 32 degrees estimated in Section 2.4. The agreement was reasonable considering the methods for manufacturing the needle.

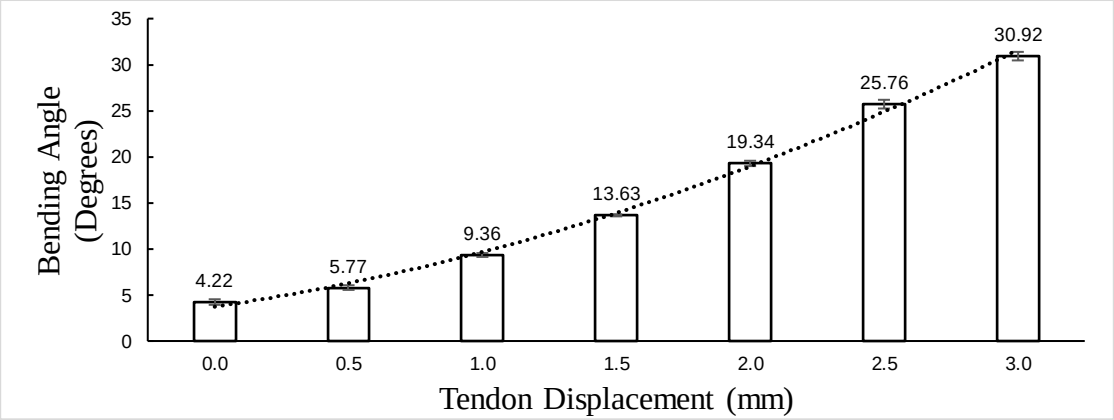

Figure 6. Angular bending of the uni-directional needle in air.

2.7.2. Needle deflection in phantom tissue

Figure 7a shows the needle deflection when inserted to a depth of 140mm into a phantom tissue. The phantom material was a polyvinylchloride (PVC) gel (M-F Manufacturing Co., Ft. Worth, TX), with a 3:1 ratio of plastic (PVC suspension) to softener that gives an indentation elastic modulus of about 25.6±0.6kPa [86] that is comparable to the modulus of normal prostate tissue (22.74 kPa).

In order to avoid the obstacle in the scenario described in Section 2.1, the needle was first inserted to a depth of 120mm, and then the tendon was pulled at a rate of 0.1mm/s while being

inserted to a depth of 140mm to reach the target. Motorized stages determined the insertion and actuation rates, and the values were set manually in an open-loop manner. Upon completion of the needle insertion task, the needle was scanned by an ultrasound device (Chison, Eco 5) similar to [87]. The needle tip's lateral and vertical positions are shown in Figure 7b and c, respectively. The 3D position of the needle tip is plotted in Figure 7d.

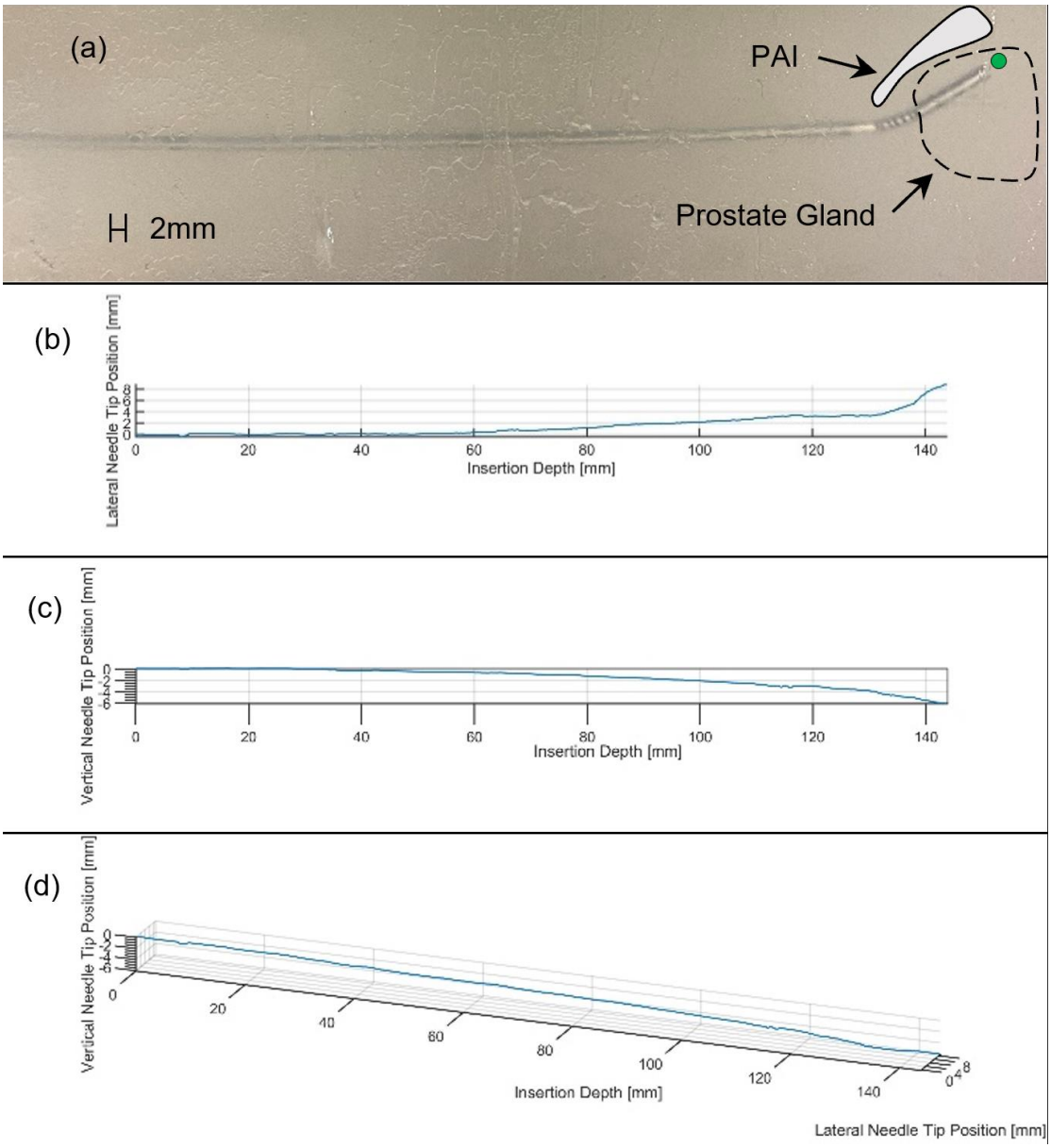

Figure 7. (a) Uni-directional needle inserted to a depth of 140mm into a phantom tissue, (b) - (d) lateral, vertical, and 3D position of the needle tip scanned by an ultrasound device, respectively.

To show the needle's capability to bend inside the phantom tissue, needle bending was measured at different tendon displacements ranging from 0.5mm to 3.0mm. The angular bending of the needle inside the phantom tissue is shown in Figure 8. Smaller needle deflection was observed inside the phantom tissue compared to the needle bending in the air (Figure 6), which was expected due to the tissue resistance.

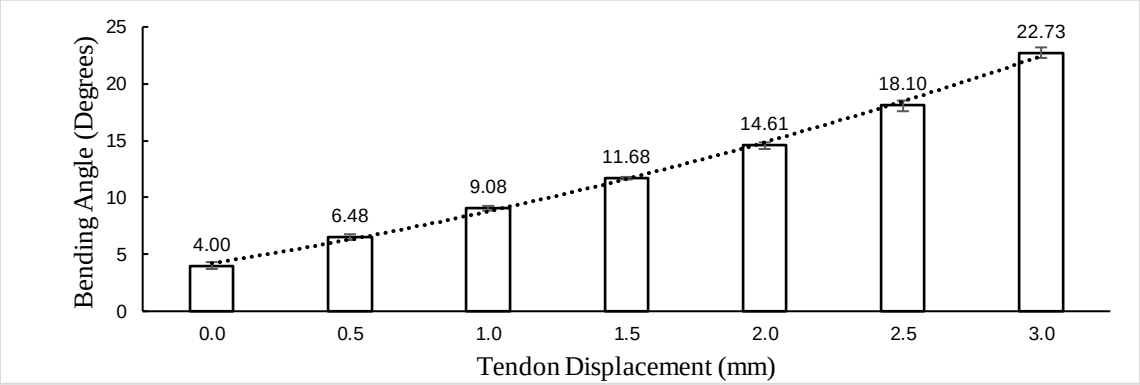

Figure 8. Angular bending of the notched needle in phantom tissue

Chapter 3. Bidirectional Steerable Active Needle for Targeted Prostate Biopsy – Design, Control, and Performance Evaluation

Section 3.1 introduces a novel design concept of a tendon-driven notched needle with a capability of bending in bidirectional. Section 3.2 describes the needle flexure section fabrication method used in this work. Section 3.3 discusses the modeling and bending calculation of the flexure section. Section 3.4 discusses the bidirectional steerable biopsy needle. The actuation system designed to actuate the flexure section of the needle is discussed in section 3.5. Finally, the results section discusses the performance of the needle.

3.1. Design concept of Bidirectional steerable needle

Figure 9 shows the design of the bidirectional robotic needle with 11.25mm long flexure section. The bidirectional notches were made on a nitinol tube (Johnson Matthey, London, UK) with an outer and inner diameter of 2.00mm and 1.47mm, respectively, and tube thickness of 0.265mm. Compared to the uni-directional notch design, bidirectional design offers more flexibility due to having thin and closer cuts. Needle insertion starts with puncturing the harder tissue which requires high forces on the needle shaft. In order to satisfy these constraints, a tube with larger outer and inner diameter was selected to increase the stiffness.

A series of six and five notches were carved on the nitinol tube towards the left and right side of the needle shaft, respectively. Regarding to the machining setup, the workspace (cut-off disc displacement along the needle's tube length) for notch creation is limited. Due to this limitation, six and five notches were the maximum number of notches that could be made on the needle to maximize the bending angle. Misalignments, in fabrication of bidirectional notches, could be a source of error in robot manipulation and control. Therefore, precise fabrication is desired, which significantly improves the controllability of the bidirectional needle, avoiding errors from misalignments and friction. With highly precise manufacturing methods, an omnidirectional compliant section might be feasible with a spiral-like design.

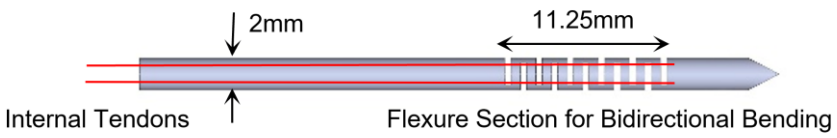

Figure 9. Schematic design of the tendon-driven bidirectional steerable needle

Figure 10a shows the bidirectional needle in bent positions. Figure 10c shows schematic of two adjacent notches with the dimensions listed in **Error! Reference source not found.**. The average cut width (h), depth (d), and distance between the notches (t) were 0.394, 1.676, and 0.582mm, respectively. The values were selected to result in bidirectional bending about ±30 degrees suitable for prostate biopsy, especially for those with larger prostates.

Table 3. Dimensions of the notches carved on the nitinol tube to fabricate the bidirectional needle. Units are in mm.

Notches on the left side	1	2	3	4	5	6
Cut Width (*h*)	0.424	0.396	0.396	0.368	0.368	0.382
Cut Depth (*d*)	1.597	1.750	1.785	1.591	1.501	1.556
Notches on the right side	1	2	3	4	5	
Cut Width (*h*)	0.41	0.396	0.417	0.389	0.389	
Cut Depth (*d*)	1.666	1.805	1.576	1.791	1.819	
Distance between the Notches (*t*)	0.711	0.596	0.642	0.558	0.626	
	0.514	0.544	0.530	0.585	0.485	

Two circular holes (diameter of about 0.25mm) were made close to the distal end of the tube on the left and right side to house two internal tendons (nitinol wire of 0.13mm diameter). The tendons were looped in and out of the holes to secure their attachment. Tension of the tendons assures bending in the direction of the notches. The notch pattern carved on the nitinol tube determines its bending properties. Figure 10c shows the range-of-motion (ROM) analysis of the bidirectional needle, reaching a large volume within the prostate gland. The prostate model and the marked targets (shown in Figure 10c) were downloaded from The Cancer Imaging Archive [88–90] for an anonymized patient with prostate cancer, undergone MRI-US fusion prostate biopsy.

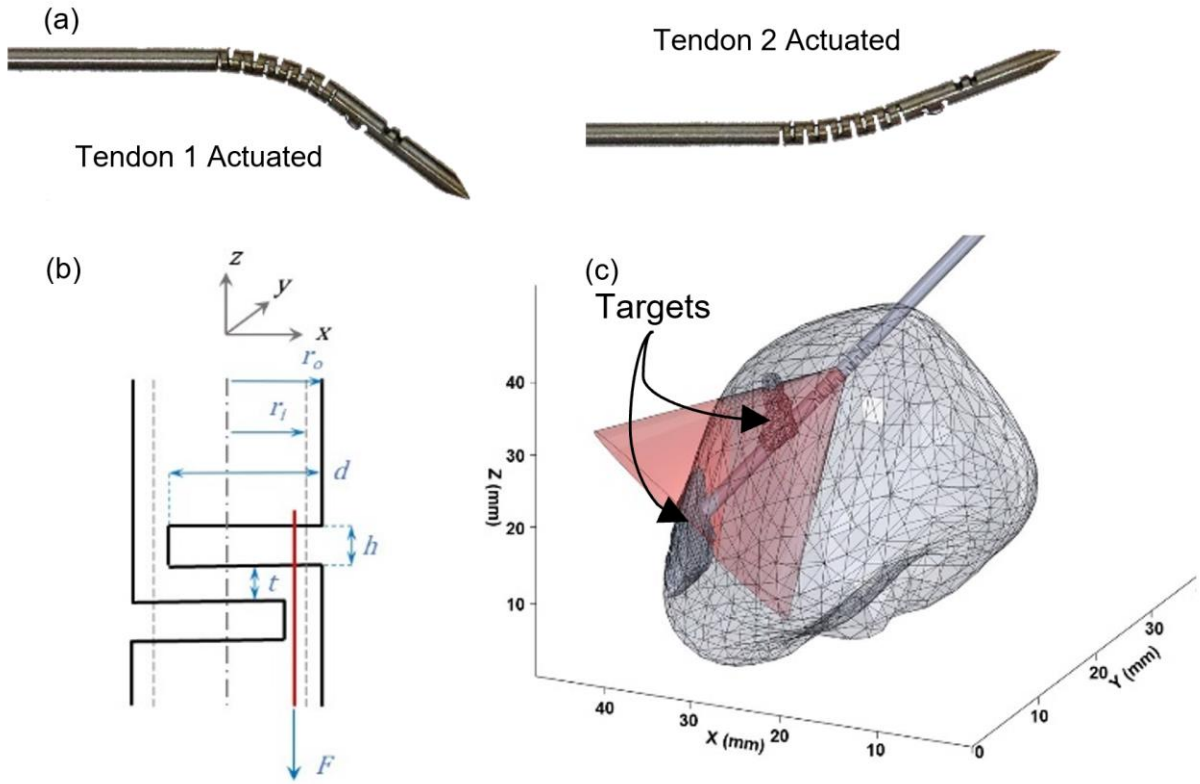

Figure 10. (a) Fabricated tool in actuated position, (b) Dimensions for modeling the flexure section, and (c) Range of motion of the bidirectional needle to reach targeted positions (darker objects) inside prostate gland.

Prostate volume of the patient is measured via MRI prostate segmentation at the time of biopsy. Each target is marked by a uroradiologist and later acquired as a single core during ultrasound-guided biopsy by a urologist. The model was used to show the bidirectional steerable needle reachability in the prostate gland.

3.2. Fabrication process

The needle-making set-up mentioned in section 2.3 was used in the fabrication process. The bidirectional notches (shown in Figure 11b) were made using cut-off disk with a thickness of 0.3mm (Gesswein & Co., Inc., Bridgeport, Connecticut). First, six thin cuts (shown in Figure 11a) with a same distance from each other were made on the one side of the tube. Then, using a same disk, five notches were made on the other side of the tube (180 degrees apart from the previous cuts). Due to the constraints of Dremel shaft length, uneven number of notches were made on the tube.

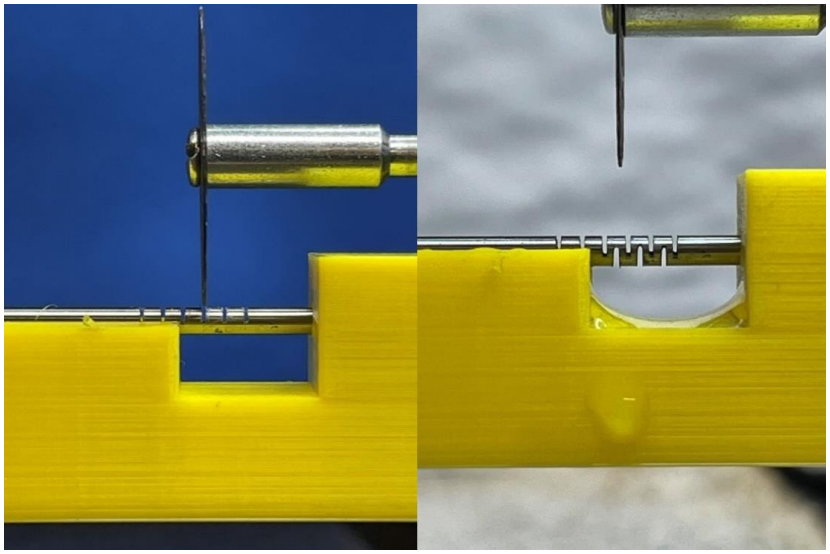

Figure 11. (a) Left side cuts (b) Right side cuts

3.3. Modeling and bending calculation

For the bidirectional needle tool, the bending angle of a flexure section (θ_{total}) with N notches is calculated by [91]:

$$\theta_{\text{total}} = \frac{N-1}{2}\theta_{\text{notch}} \quad (6)$$

where θ_{notch} is the bending angle of a single notch, which can be calculated using Castigliano's second theorem as:

$$\theta_{\text{notch}} = \frac{\partial U}{\partial M_r} \quad (7)$$

where U is the total internal energy and M_r is the moment at the cross section, calculated using the following equations:

$$U = \frac{1}{2}\int_{-(d-r_o)}^{d-r_o}\int_{-\frac{t}{2}}^{\frac{t}{2}}\frac{M_r(x)^2 z^2 w(x)}{EI^2(x)}\,dzdx \quad (8)$$

$$M_r(x) = M - F_1 \times (d - r_o - x) \quad (9)$$

where d is the depth of the notch, t is the distance between two notches, r_o and r_i are the outer and inner radii of the nitinol tube, respectively, E is the young modulus, and F_1 is the force applied on each notch. The effects of gravity aren't considered in this work. w(x), I(x), and M are width of the section, second moment of area with respect to the y-axis, and the moment applied to the section, found by the following three equations:

$$w(x) = \sqrt{r_o^2 - x^2} - \sqrt{r_i^2 - x^2} \quad (10)$$

$$I(x) = \frac{1}{12}t^3 w(x) \quad (11)$$

$$M = F_1 \times (d - (r_o - r_i) - \frac{t_d}{2}) \quad (12)$$

where t_d is the tendon diameter. For a needle with the average dimensions (in which F_1 is used to calculate the average bending for a single notch) listed in **Error! Reference source not found.**, we have estimated about 4.90 degrees of bending for each notch. This will result in 28.58 and 19.87 degrees of bending towards left and right directions, respectively. Since this is an average bending per notch, the theoretical values will vary depending on this approximation.

Table 4. Average dimensions of the bidirectional needle.

r_o (mm)	r_i (mm)	d (mm)	t_d (mm)	t (mm)	N	F_1 (N)	E (GPa)
1	0.735	1.676	0.13	0.582	11	0.981	24.3

3.4. Bidirectional steerable biopsy needle

3.4.1. Design concept of bidirectional steerable needle

The same bidirectional notch design concept with different dimensions was utilized to reach higher flexibility. The biopsy needle design features a 10.93mm long compliant flexure section (shown in Figure 12a) for bidirectional bending. The flexure section is actuated via two internal tendons (nitinol wires of 0.13mm diameter). The same superelastic nitinol tube (Johnson Matthey, London, UK) with an outer and inner diameter of 2.00 and 1.47mm, respectively, and a tube thickness of 0.265mm was used. The flexure section was made 40mm from the needle tip to contain the biopsy mechanism. Six notches are carved on the nitinol tube's left and right sides to create a compliant flexure section with bidirectional bending capabilities.

Figure 12b shows a schematic view of two adjacent notches with the dimensions listed in **Error! Reference source not found.**. The average cut width (h), depth (d), and distance between the notches (t) are 0.41, 1.56, and 0.55mm, respectively. The values are selected to result in bidirectional bending of about ±35 degrees suitable for prostate biopsy, especially for patients with larger prostate glands.

Two additional small notches (diameter of about 0.25mm) are fabricated on the nitinol tube on the left and right sides towards the distal end of the flexure section for tendon attachments. Figure 12c shows tendon attachment for one side.

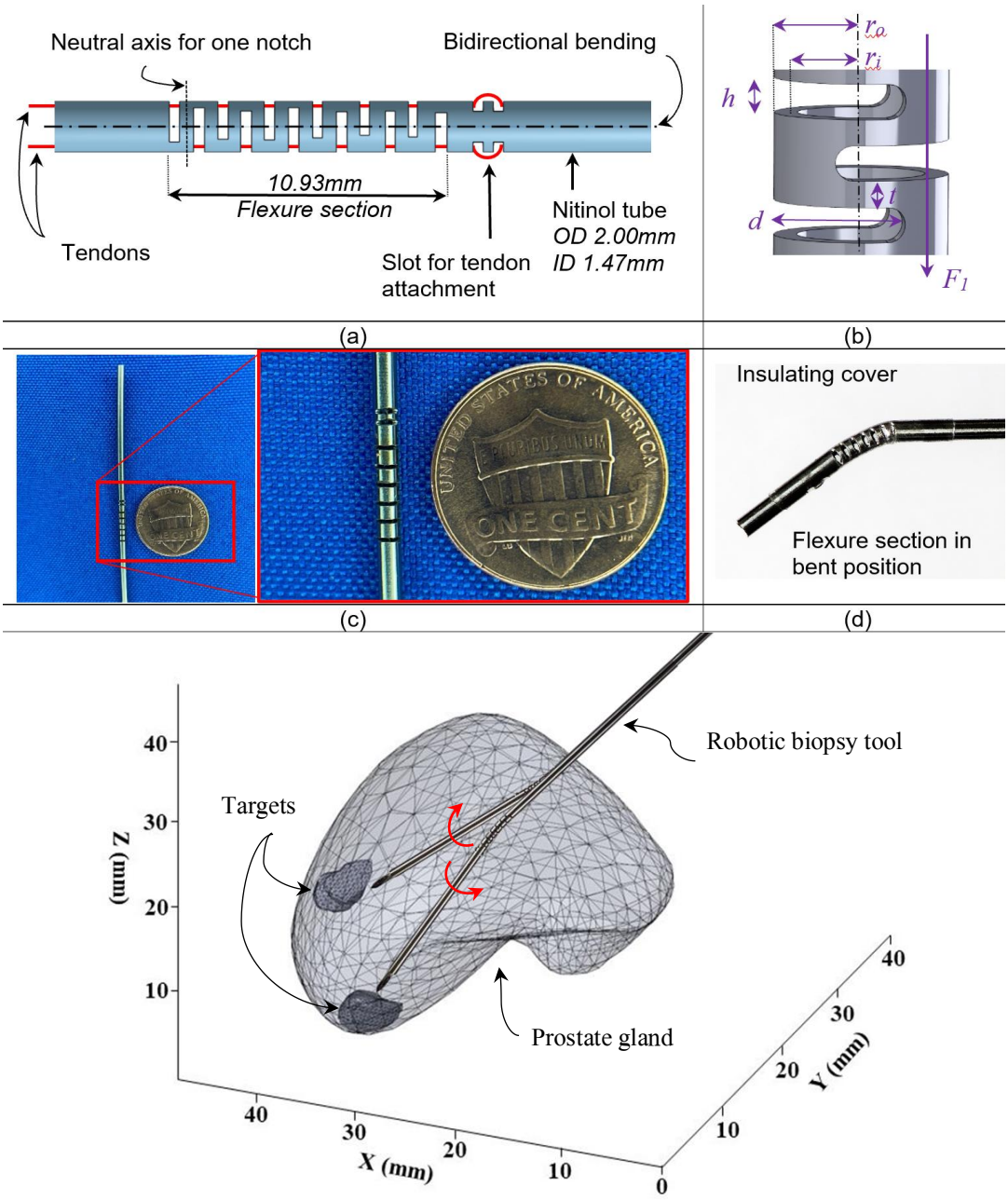

Figure 12. (a) Design of the tendon-driven bidirectional needle and its compliant flexure section, (b) model parameters for the flexure section, (c) fabricated bidirectional needle with six notches

and a small slot for tendon attachment on each side (one side is shown), (d) flexure section in bent position with heat shrink cover, and (e) range of motion of the bidirectional needle to reach targets inside the prostate gland.

The notch pattern carved on the nitinol tube determines its bending properties. Figure 12e shows the range-of-motion (ROM) analysis of the bidirectional needle, reaching a target area within the prostate gland. The prostate model is used here to analyze the bidirectional biopsy needle's reachability in prostate gland.

3.4.2. Modeling of bidirectional biopsy needle

Modeling of the bidirectional biopsy needle was used same equations mentioned in section 3.3. For the average dimensions listed in **Error! Reference source not found.** (in which F_1 is used to calculate the average bending for a single notch), we have estimated about 7.4 degrees of bending for each notch. This will result in 37.0 degrees of bending. It should be noted that Equation 10 gives same values for angular bending. Since this is an average bending per notch, the theoretical values will vary depending on this approximation.

Table 5. Dimensions of the notches carved on the nitinol tube to fabricate the bidirectional needle. Units are in mm.

Notches on the left side (from proximal to distal end)	1	2	3	4	5	6
Cut Width (*h*)	0.356	0.383	0.383	0.412	0.411	0.411
Cut Depth (*d*)	1.407	1.342	1.443	1.525	1.497	1.601
Notches on the right side (from proximal to distal end)	1	2	3	4	5	6
Cut Width (*h*)	0.466	0.383	0.425	0.425	0.438	0.438
Cut Depth (*d*)	1.547	1.616	1.591	1.74	1.618	1.739
Distance between the Notches (*t*)	0.548	0.521	0.48	0.493	0.535	0.534
	0.548	0.493	0.63	0.52	0.7	0.548

3.4.3. Biopsy Mechanism

A biopsy tray, detached from TEMNO Evolution® Biopsy Device from Merit Medical Systems, Inc. (shown in Figure 13a), is attached to a flexible guidewire and inserted inside the bidirectional needle tube as a stylet. The biopsy tray features a sampling notch length of 20mm with a sharp trocar tip for easy insertion. A slight chamfer is made on the proximal end of the biopsy tray for the flexible wire to get epoxied without an increase in the overall diameter. Figure 13b shows the integration of the biopsy mechanism with the bidirectional needle. Figure 13c shows the fabricated prototype and its ability to manually deploy the biopsy tray in bent positions.

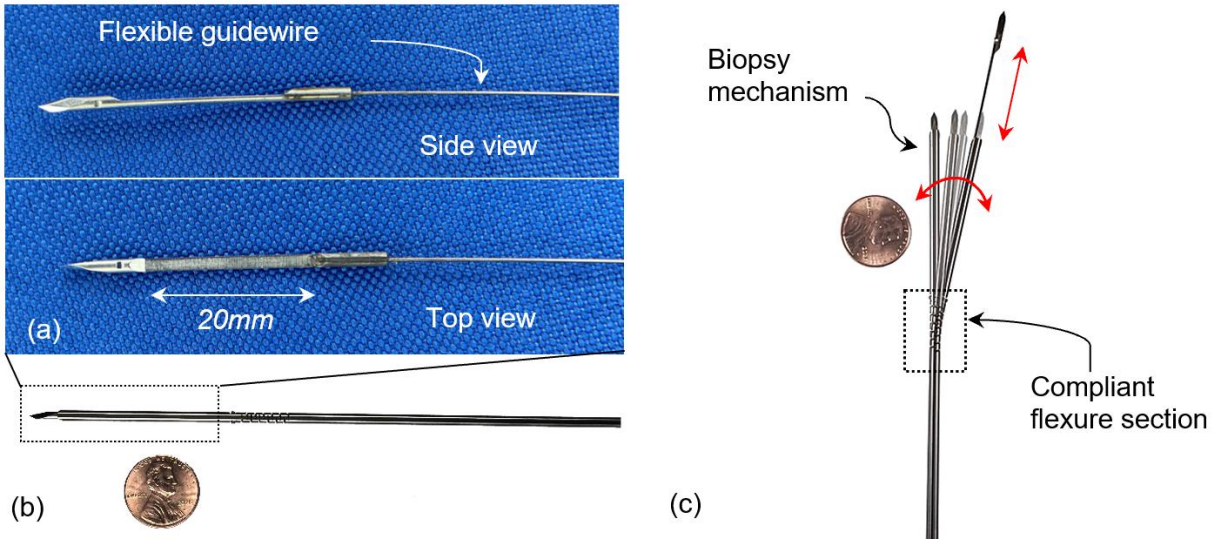

Figure 13. Integration of biopsy mechanism with the bidirectional needle: (a) biopsy tray and flexible guidewire, (b) fabricated prototype, and (c) operation of the biopsy mechanism (bending at flexure section and employing biopsy tray for extraction of tissue samples).

3.5. Robotic needle actuation system

The actuation setup, shown in Figure 14 consisting of two 0.5W Maxon DC motors RE 8 Ø8 mm, Precious Metal Brushes with 8mm diameter lead screw drives (GP 8 S Ø8mm, Metric spindle, M3 x 0.5), and encoders (MR, Type S, 100CPT), is used for actuating the needle. Two holders are designed, and 3D printed to hold the Maxon motors and the lead screws. The first holder (housing the spindle on the lead screw) is mounted on a linear rail guide to translate rotational movement of the motor shaft to linear movement. The second holder is stationary, keeping the position of the motor. The free end of the tendon is fixed on the first holder. The tendon is threaded through the midpoint of the holder to ensure colinear movement.

The motors are controlled via EPOS Command Library functions that use input values called increments. Through measurement, it is determined that 100,000 increments are equal to 1 mm of linear displacement of the lead screw attached to the motors. The program uses incrementation to tighten the tendons attached to the motors and decrementation to loosen the tendons. The motors are actuated by 50,000 increments, or 0.5 mm, depending on the assumed location of the tip. If the bidirectional needle is in a neutral position at the start, the tendon responsible for bending the tip to the right will be tightened 0.5 mm by the motor, in this case the right motor. If the bidirectional needle is bent to the left at the start, then instead of tightening the right tendon, the left tendon will be loosened by 0.5 mm instead. Due to the mounting positions of the tendons on the bidirectional needle, there is no need for the loosening tendon (in this example, the left tendon) to loosen once the bidirectional needle is bent past the neutral position. More clearly, and still using the same example, if the bidirectional needle is being bent to the right the left tendon does not need to be loosened once the bidirectional needle has bent to the right of the neural point. Lastly, if the bidirectional needle is bent to the right at the start, then the right tendon

will be tightened by 0.5 mm like in the case of a neutral starting point. However, if the bidirectional needle is already bent to the point where it is nearing its maximum limit, then the incrementation will not ensue, and the user will receive a message displayed on screen that the maximum bending angle has been achieved. This is to protect the bidirectional needle from unnecessary stress.

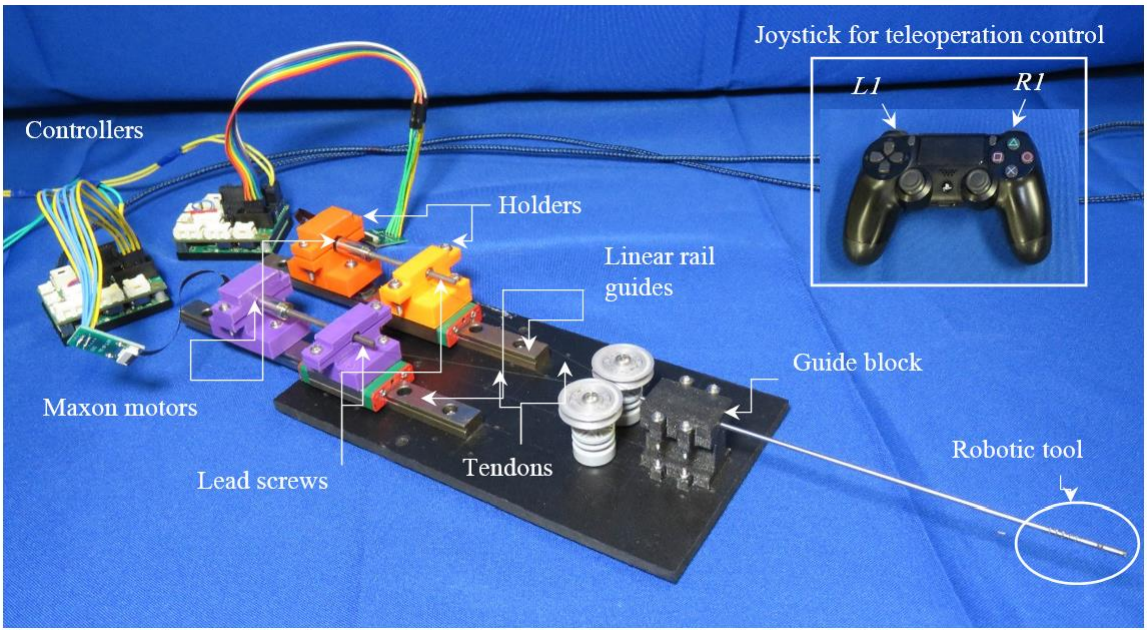

Figure 14. Actuation system to realize bending on the bidirectional needle

3.6. Results

3.6.1. Bending angle control via tendon-displacement

The Maxon motors are used in this section to realize bending at the tip of the bidirectional needle using tendon displacement control. Figure15**Error! Reference source not found.** shows the angular bending of the bidirectional needle using tendon displacement control. The error bars are calculated to show the higher and lower values in three trials. Maximum bending angle via displacement control using the Maxon motors is 31.67 degrees, which is comparable with tendon tension control from Section 3.3 (shown in Figure15). Once the maximum bending angle is reached, the motors are stopped to prevent plastic deformation or fractures within the bidirectional needle. In this work, each trial starts with pulling the tendons taut so the hysteresis effect from the nitinol tendons is neglected.

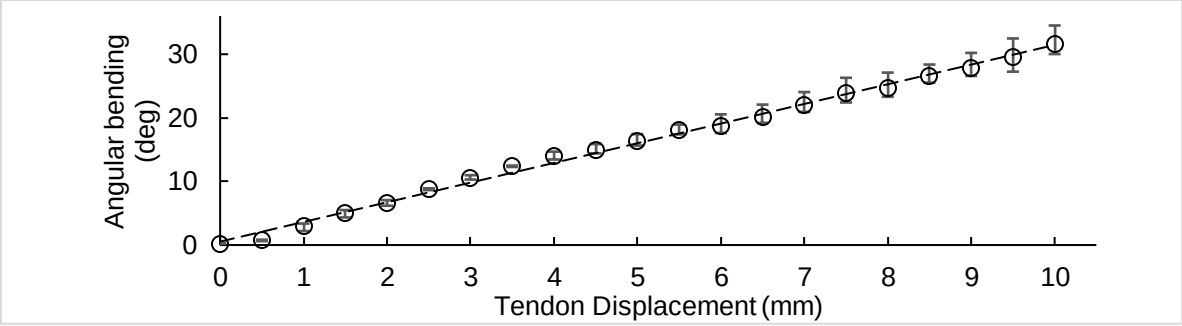

Figure 15. Angular deflection of the bidirectional needle via actuation of internal tendon.

3.6.2. Bending capability evaluation for targeted prostate biopsy

To evaluate the capability of the bidirectional needle to produce sufficient bidirectional bending to reach the target positions inside a prostate gland, an experimental setup (shown in Figure 16) is developed with assigned target positions inside a pelvis male model (BARSCI, Rochester, NY). The targets are 3D printed and mounted inside the pelvis model to represent geometric relationships. Top view (shown in Figure 16 insert) is provided to the user via a camera

placed on top of the pelvis model. It is shown that the range of motion provided by the bidirectional bending of the needle is sufficient to cover the marked targets (spheres on the endpoints of the 3D print). The targets are randomly generated to demonstrate the workspace of the bidirectional biopsy needle. The bidirectional needle and the actuation system are intended to be installed on a needle insertion robotic system (presented in our previous publications [89,92], to enable axial needle insertion and rotation for 3D targeting inside the prostate gland.

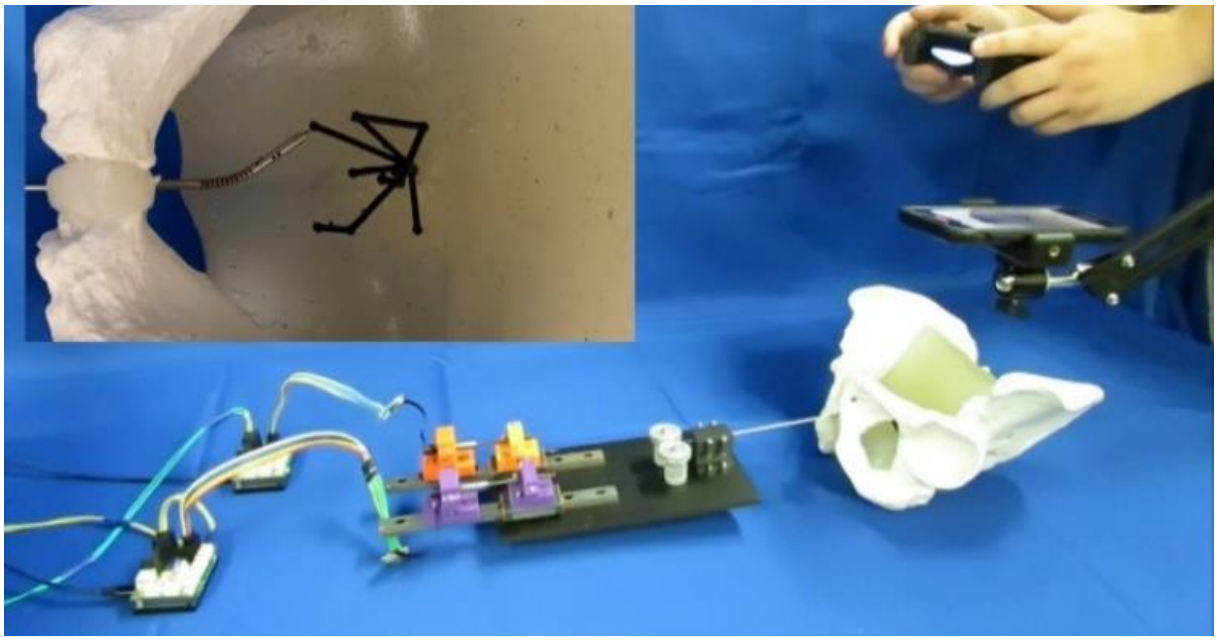

Figure 16. Bidirectional needle bending to reach marked targets inside a prostate gland.

3.6.3. Extraction of biopsy samples from phantom tissue

The capability of the bidirectional needle to bend inside a phantom tissue and extract a phantom tissue is evaluated and shown in this section. The bidirectional needle is bent inside the phantom via the actuation and control system, shown in previous section, and then the biopsy mechanism is deployed manually to trap a phantom tissue. Figure 17a shows the bidirectional needle in a bent position inside the phantom tissue. Figure 17b to d show the biopsy mechanism in fully-open, half- and fully-closed positions, respectively.

The workflow of biopsy mechanism is explained. The needle was inserted into the tissue when the tray was inside the bidirectional needle (shown in Figure 17b). Then the actuation system was applied to align the needle tip towards the target. Before reaching the target, needle insertion was stopped, and tray was pushed until reaching target area. While the tray was held at the same position manually, the needle tube was inserted to cut the tissue. Once the tissue resides in the tray, the stress of the tendon was released, and the needle was retracted. Figure 17c shows the fabricated prototype and its ability to manually open and close the biopsy tray in bent positions.

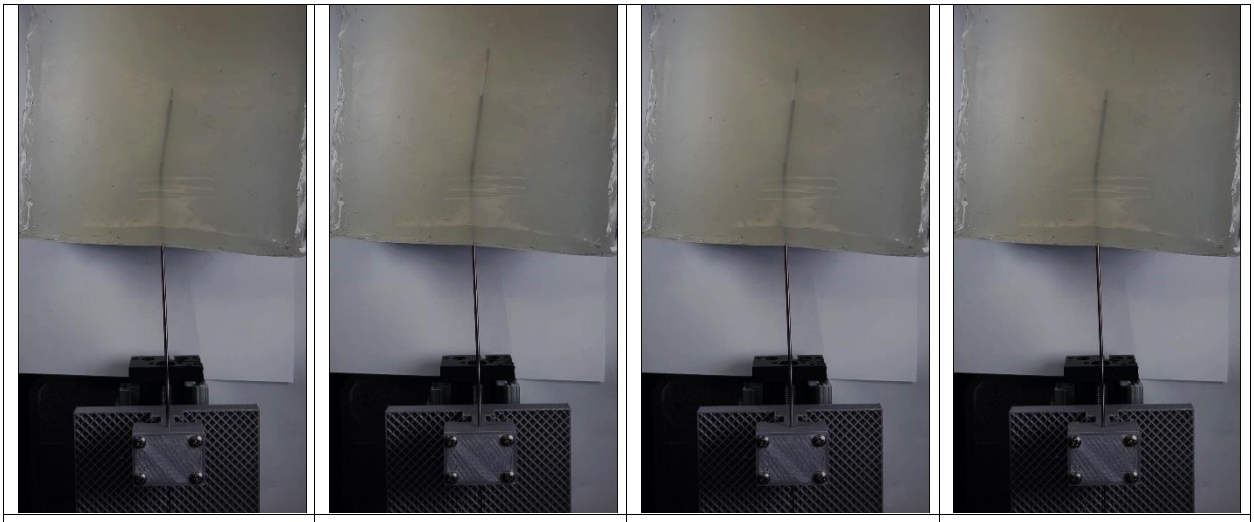

(a) (b) (c) (d)

Figure 17. The bidirectional needle and biopsy mechanism used to (a) realize a desired bending inside a phantom tissue, (b) deploy the biopsy tray, (c) pull the biopsy tray back to trap the tissue sample, and (d) close the tray to cut the tissue sample.

CONCLUSION

In summary, this work first presented a tendon-driven notched needle with unidirectional bending capability to overcome the obstacles in needle placement in HDR BT for patients with PAI. The needle was designed and fabricated to bend inside the patient at a maximum bending angle of 30 degrees to pass a pubic arch with 10mm of overlap with the prostate gland. The flexure section of the needle was fabricated by carving several notches on a nitinol tube, and uni-directional bending was realized via actuation of an internal tendon. The active needle is also able reach the out-of-plane target positions via axial rotation.

Second, a different notch pattern was introduced to bend the needle bidirectionally, equipped with a core biopsy mechanism. The flexure section was modeled using Castigliano's theory. Bending capability of the needle was evaluated in air and tissue. Lastly, the biopsy extraction mechanism was proven to be feasible when the needle was in bent position.

The study concludes that active tendon-driven notched needles provide solution for s with PAI, for whom HDR BT may come with additional challenges. It was also concluded that the tendon-driven notched needles equipped with biopsy traction mechanism can extract multiple significant cancerous samples with fewer insertions. Utilization of the tendon-driven notched needles for prostate biopsy provides an effective targeted biopsy method compared to the conventional systematic (12-core) biopsy. The tendon-driven notched needles when integrated with image-guided robotic systems can improve the outcome of MRI-US fusion prostate biopsy.

FUTURE WORK

Integrating the tendon-driven notched needles with the robotic image-guided needle insertion system to test needle steerability in prostate-like tissue, is left for future studies. Higher needle deflection is possible by improving the fabrication process of the flexure section. Force is one of the crucial factors in needle steering inside soft tissue. However, this study did not account for the needle insertion and actuation forces. Thus, a hybrid force and position closed-loop control system can be implemented to accurately control the notched needles in tissue.

REFERENCES

[1] 2022, “Prostate Cancer: Statistics,” Cancer.Net. [Online]. Available: https://www.cancer.net/cancer-types/prostate-cancer/statistics.

[2] Tarone, R. E., Chu, K. C., and Brawley, O. W., 2000, “Implications of Stage-Specific Survival Rates in Assessing Recent Declines in Prostate Cancer Mortality Rates.,” Epidemiology, **11**(2), pp. 167–170.

[3] Thompson, I. M., Pauler, D. K., Goodman, P. J., Tangen, C. M., Lucia, M. S., Parnes, H. L., Minasian, L. M., Ford, L. G., Lippman, S. M., Crawford, E. D., Crowley, J. J., and Coltman, C. A. J., 2004, “Prevalence of Prostate Cancer among Men with a Prostate-Specific Antigen Level < or =4.0 Ng per Milliliter.,” N. Engl. J. Med., **350**(22), pp. 2239–2246.

[4] Kelloff, G. J., Choyke, P., and Coffey, D. S., 2009, “Challenges in Clinical Prostate Cancer: Role of Imaging,” Am. J. Roentgenol., **192**(6), pp. 1455–1470.

[5] Kasivisvanathan, V., Stabile, A., Neves, J. B., Giganti, F., Valerio, M., Shanmugabavan, Y., Clement, K. D., Sarkar, D., Philippou, Y., Thurtle, D., Deeks, J., Emberton, M., Takwoingi, Y., and Moore, C. M., 2019, “Magnetic Resonance Imaging-Targeted Biopsy Versus Systematic Biopsy in the Detection of Prostate Cancer: A Systematic Review and Meta-Analysis.,” Eur. Urol., **76**(3), pp. 284–303.

[6] Ahdoot, M., Wilbur, A. R., Reese, S. E., Lebastchi, A. H., Mehralivand, S., Gomella, P. T., Bloom, J., Gurram, S., Siddiqui, M., Pinsky, P., Parnes, H., Linehan, W. M., Merino, M., Choyke, P. L., Shih, J. H., Turkbey, B., Wood, B. J., and Pinto, P. A., 2020, “MRI-Targeted, Systematic, and Combined Biopsy for Prostate Cancer Diagnosis,” N. Engl. J. Med., **382**(10), pp. 917–928.

[7] Oto, A., 2019, “Navigating the Challenges of Targeting Accuracy and Tumor Heterogeneity in Targeted Prostate Biopsy,” Radiology, **291**(1), pp. 90–91.

[8] Anandadas, C. N., Clarke, N. W., Davidson, S. E., O’Reilly, P. H., Logue, J. P., Gilmore, L., Swindell, R., Brough, R. J., Wemyss-Holden, G. D., Lau, M. W., Javle, P. M., Ramani, V. A. C., Wylie, J. P., Collins, G. N., Brown, S., and Cowan, R. A., 2011, “Early Prostate Cancer--Which Treatment Do Men Prefer and Why?,” BJU Int., **107**(11), pp. 1762–1768.

[9] Gwede, C. K., Pow-Sang, J., Seigne, J., Heysek, R., Helal, M., Shade, K., Cantor, A., and Jacobsen, P. B., 2005, “Treatment Decision-Making Strategies and Influences in Patients with Localized Prostate Carcinoma.,” Cancer, **104**(7), pp. 1381–1390.

[10] Merrick, G., Zelefsky, M., Sylvester, J., Nag, S., and Bice, W., 2007, “American Brachytherapy Society (ABS) Prostate Low-Dose Rate Task Group Guidelines.”

[11] Yu, Y., Anderson, L. L., Li, Z., Mellenberg, D. E., Nath, R., Schell, M. C., Waterman, F. M., Wu, A., and Blasko, J. C., 1999, “Permanent Prostate Seed Implant Brachytherapy: Report of the American Association of Physicists in Medicine Task Group No. 64,” Med. Phys., **26**(10), pp. 2054–2076.

[12] Merrick, G. S., Butler, W. M., Dorsey, A. T., and Walbert, H. L., 1998, “Influence of Timing on the Dosimetric Analysis of Transperineal Ultrasound-Guided, Prostatic Conformal Brachytherapy.,” Radiat. Oncol. Investig., **6**(4), pp. 182–190.

[13] Nag, S., Beyer, D., Friedland, J., Grimm, P., and Nath, R., 1999, “American Brachytherapy Society (ABS) Recommendations for Transperineal Permanent Brachytherapy of Prostate Cancer.,” Int. J. Radiat. Oncol. Biol. Phys., **44**(4), pp. 789–799.

[14] Stone, N. N., Roy, J., Hong, S., Lo, Y. C., and Stock, R. G., 2002, “Prostate Gland Motion and Deformation Caused by Needle Placement during Brachytherapy,” Brachytherapy,

1(3), pp. 154–160.
[15] Lee, S., Rodney, E., Traughber, B., Biswas, T., Colussi, V., and Podder, T., 2017, "Evaluation of Interfractional Variation of Organs and Displacement of Catheters during High-Dose-Rate Interstitial Brachytherapy for Gynecologic Malignancies," Brachytherapy, **16**(6), pp. 1192–1198.
[16] Mai, K. T., and Veinot, J. P., 2008, "Re: Central Zone Carcinoma of the Prostate Gland: A Distinct Tumor Type with Poor Prognostic Features: R. J. Cohen, B. A. Shannon, M. Phillips, R. E. Moorin, T. M. Wheeler and K. L. Garrett J Urol 2008; 179: 1762-1767.," J. Urol., **180**(6), pp. 2714; author reply 214-5.
[17] Morton, G. C., and Hoskin, P. J., 2019, "Single Fraction High-Dose-Rate Brachytherapy: Too Good to Be True?," Int. J. Radiat. Oncol. Biol. Phys., **104**(5), pp. 1054–1056.
[18] Martin, J. M., Handorf, E. A., Kutikov, A., Uzzo, R. G., Bekelman, J. E., Horwitz, E. M., and Smaldone, M. C., 2014, "The Rise and Fall of Prostate Brachytherapy: Use of Brachytherapy for the Treatment of Localized Prostate Cancer in the National Cancer Data Base," Cancer, **120**(14), pp. 2114–2121.
[19] Orio, P. F., Nguyen, P. L., Buzurovic, I., Cail, D. W., and Chen, Y. W., 2016, "The Decreased Use of Brachytherapy Boost for Intermediate and High-Risk Prostate Cancer despite Evidence Supporting Its Effectiveness," Brachytherapy, **15**(6), pp. 701–706.
[20] Popescu, T., Kacsó, A. C., Pisla, D., and Kacsó, G., 2015, "Brachytherapy next Generation: Robotic Systems.," J. Contemp. Brachytherapy, **7**(6), pp. 510–514.
[21] Wallner, K., Ellis, W., Russell, K., Cavanagh, W., and Blasko, J., 1999, "Use of TRUS to Predict Pubic Arch Interference of Prostate Brachytherapy.," Int. J. Radiat. Oncol. Biol. Phys., **43**(3), pp. 583–585.
[22] Nickers, P., Thissen, B., Jansen, N., and Deneufbourg, J. M., 2006, "192Ir or 125I Prostate Brachytherapy as a Boost to External Beam Radiotherapy in Locally Advanced Prostatic Cancer: A Dosimetric Point of View," Radiother. Oncol., **78**(1), pp. 47–52.
[23] Bellon, J., Wallner, K., Ellis, W., Russell, K., Cavanagh, W., and Blasko, J., 1999, "Use of Pelvic CT Scanning to Evaluate Pubic Arch Interference of Transperineal Prostate Brachytherapy.," Int. J. Radiat. Oncol. Biol. Phys., **43**(3), pp. 579–581.
[24] Tincher, S. A., Kim, R. Y., Ezekiel, M. P., Zinsli, T., Fiveash, J. B., Raben, D. A., Bueschen, A. J., and Urban, D. A., 2000, "Effects of Pelvic Rotation and Needle Angle on Pubic Arch Interference during Transperineal Prostate Implants.," Int. J. Radiat. Oncol. Biol. Phys., **47**(2), pp. 361–363.
[25] Ryu, B., Bax, J., Edirisinge, C., Lewis, C., Chen, J., D'Souza, D., Fenster, A., and Wong, E., 2012, "Prostate Brachytherapy with Oblique Needles to Treat Large Glands and Overcome Pubic Arch Interference," Int. J. Radiat. Oncol. Biol. Phys., **83**(5), pp. 1463–1472.
[26] de Jong, T. L., van de Berg, N. J., Tas, L., Moelker, A., Dankelman, J., and van den Dobbelsteen, J. J., 2018, "Needle Placement Errors: Do We Need Steerable Needles in Interventional Radiology?," Med. Devices (Auckl)., **11**, pp. 259–265.
[27] Konh, B., Honarvar, M., Darvish, K., and Hutapea, P., 2017, "Simulation and Experimental Studies in Needle-Tissue Interactions.," J. Clin. Monit. Comput., **31**(4), pp. 861–872.
[28] De Jong, T. L., van de Berg, N. J., Tas, L., Moelker, A., Dankelman, J., and van den Dobbelsteen, J. J., 2017, "Needle Placement Errors: Do We Need Steerable Needles in Interventional Radiology?," Med. Devices Evid. Res., **37**(3), pp. 259–265.

[29] Matheson, E., Secoli, R., Burrows, C., Leibinger, A., and y Baena, F., 2018, "Cyclic Motion Control for Programmable Bevel-Tip Needles to Reduce Tissue Deformation," J. Med. Robot. Res., **04**.
[30] Scali, M., Pusch, T. P., Breedveld, P., and Dodou, D., 2017, "Needle-like Instruments for Steering through Solid Organs: A Review of the Scientific and Patent Literature," Proc. Inst. Mech. Eng. Part H J. Eng. Med., **231**(3), pp. 250–265.
[31] Berg, N., van Gerwen, D., Dankelman, J., and Dobbelsteen, J., 2014, "Design Choices in Needle Steering—A Review," IEEE/ASME Trans. Mechatronics, **20**.
[32] Yang, F., Babaiasl, M., and Swensen, J., 2018, "Fracture-Directed Steerable Needles," J. Med. Robot. Res., **04**.
[33] Carriere, J., Khadem, M., Rossa, C., Usmani, N., Sloboda, R., and Tavakoli, M., 2019, "Event-Triggered 3D Needle Control Using a Reduced-Order Computationally Efficient Bicycle Model in a Constrained Optimization Framework," J. Med. Robot. Res., **04**(01), p. 1842004.
[34] Tsumura, R., Takishita, Y., and Iwata, H., 2019, "Needle Insertion Control Method for Minimizing Both Deflection and Tissue Damage," J. Med. Robot. Res., **04**(01), p. 1842005.
[35] Cowan, N. J., Goldberg, K., Chirikjian, G. S., Fichtinger, G., Alterovitz, R., Reed, K. B., Kallem, V., Park, W., Misra, S., and Okamura, A. M., 2011, "Robotic Needle Steering: Design, Modeling, Planning, and Image Guidance," *Surgical Robotics: Systems Applications and Visions*.
[36] Su, H., Li, G., Rucker, D. C., Webster III, R. J., and Fischer, G. S., 2016, "A Concentric Tube Continuum Robot with Piezoelectric Actuation for MRI-Guided Closed-Loop Targeting," Ann. Biomed. Eng., **44**(10), pp. 2863–2873.
[37] Kuhle, W. G., "Biopsy Needle with Flared Tip."
[38] D. Kraft and J. Hole., "Device and Method for Rapid Aspiration and Collection of Body Tissue from within an Enclosed Body Space."
[39] J. S. Melsheimer, "Deflectable Biopsy Device."
[40] B. Arvanaghi, "Bendable Needle Assembly."
[41] Reed, K. B., Majewicz, A., Kallem, V., Alterovitz, R., Goldberg, K., Cowan, N. J., and Okamura, A. M., 2011, "Robot-Assisted Needle Steering," IEEE Robot. Autom. Mag., **18**(4), pp. 35–46.
[42] Wedlick, T. R., and Okamura, A. M., 2009, "Characterization of Pre-Curved Needles for Steering in Tissue.," *Annual International Conference of the IEEE Engineering in Medicine and Biology Society*, pp. 1200–1203.
[43] Okazawa, S., Ebrahimi, R., Chuang, J., Salcudean, S. E., and Rohling, R., 2005, "Hand-Held Steerable Needle Device," IEEE/ASME Trans. Mechatronics, **10**(3), pp. 285–296.
[44] Swaney, P. J., Burgner, J., Gilbert, H. B., and Webster, R. J., 2013, "A Flexure-Based Steerable Needle: High Curvature with Reduced Tissue Damage.," IEEE Trans. Biomed. Eng., **60**(4), pp. 906–909.
[45] Webster, R. J., Romano, J. M., and Cowan, N. J., 2009, "Mechanics of Precurved-Tube Continuum Robots," IEEE Trans. Robot., **25**(1), pp. 67–78.
[46] Sears, P., and Dupont, P., 2006, "A Steerable Needle Technology Using Curved Concentric Tubes," IEEE Int. Conf. Intell. Robot. Syst., pp. 2850–2856.
[47] Abolhassani, N., Patel, R., and Moallem, M., 2007, "Needle Insertion into Soft Tissue: A Survey," Med. Eng. Phys., **29**(4), pp. 413–431.

[48] Misra, S., Reed, K. B., Schafer, B. W., Ramesh, K. T., and Okamura, A. M., 2010, "Mechanics of Flexible Needles Robotically Steered through Soft Tissue.," Int. J. Rob. Res., **29**(13), pp. 1640–1660.
[49] Webster, R. J., Kim, J. S., Cowan, N. J., Chirikjian, G. S., and Okamura, A. M., 2006, "Nonholonomic Modeling of Needle Steering," *International Journal of Robotics Research*.
[50] Rossa, C., and Tavakoli, M., 2017, "Issues in Closed-Loop Needle Steering," Control Eng. Pract., **62**(March), pp. 55–69.
[51] Haddadi, A., Goksel, O., Salcudean, S. E., and Hashtrudi-Zaad, K., 2010, "On the Controllability of Dynamic Model-Based Needle Insertion in Soft Tissue," *2010 Annual International Conference of the IEEE Engineering in Medicine and Biology Society, EMBC'10*, Buenos Aires, Argentina, 8/31/2010.
[52] Ayvali, E., Liang, C. P., Ho, M., Chen, Y., and Desai, J. P., 2012, "Towards a Discretely Actuated Steerable Cannula for Diagnostic and Therapeutic Procedures," Int. J. Rob. Res., **31**(5), pp. 588–603.
[53] Ryu, S. C., Renaud, P., Black, R. J., Daniel, B. L., and Cutkosky, M. R., 2011, "Feasibility Study of an Optically Actuated MR-Compatible Active Needle," *IEEE/RSJ International Conference on Intelligent Robots and Systems*, Ieee, pp. 2564–2569.
[54] van de Berg, N. J., Dankelman, J., and van den Dobbelsteen, J. J., 2015, "Design of an Actively Controlled Steerable Needle with Tendon Actuation and FBG-Based Shape Sensing," Med. Eng. Phys., **37**(6), pp. 617–622.
[55] Gerboni, G., Greer, J. D., Laeseke, P. F., Hwang, G. L., and Okamura, A. M., 2017, "Highly Articulated Robotic Needle Achieves Distributed Ablation of Liver Tissue," IEEE Robot. Autom. Lett., **2**(3), pp. 1367–1374.
[56] Chitalia, Y., Deaton, N. J., Jeong, S., Rahman, N., and Desai, J. P., 2020, "Towards FBG-Based Shape Sensing for Micro-Scale and Meso-Scale Continuum Robots with Large Deflection," IEEE Robot. Autom. Lett., **5**(2), pp. 1712–1719.
[57] York, P. A., Swaney, P. J., Gilbert, H. B., and Webster, R. J., 2015, "A Wrist for Needle-Sized Surgical Robots," *IEEE International Conference on Robotics and Automation*, pp. 1776–1781.
[58] Varnamkhasti, Z. K., and Konh, B., 2020, "Compact 3D-Printed Active Flexible Needle for Percutaneous Procedures," Surg. Innov., **27**(4), pp. 402–405.
[59] Varnamkhasti, Z. K., and Konh, B., 2020, "Design, Fabrication, and Testing of a Flexible Three-Dimensional Printed Percutaneous Needle with Embedded Actuators," ASME J. Med. Devices, **15**(2), p. 021007 (10 pages).
[60] Haga, Y., Muyari, Y., Goto, S., Matsunaga, T., and Esashi, M., 2011, "Development of Minimally Invasive Medical Tools Using Laser Processing on Cylindrical Substrates," Electr. Eng. Japan (English Transl. Denki Gakkai Ronbunshi), **176**(1), pp. 65–74.
[61] Ryu, S. C., Quek, Z. F., Koh, J. S., Renaud, P., Black, R. J., Moslehi, B., Daniel, B. L., Cho, K. J., and Cutkosky, M. R., 2015, "Design of an Optically Controlled MR-Compatible Active Needle," IEEE Trans. Robot., **31**(1), pp. 1–11.
[62] Karthikeyan, R., Sigmund, K., Park, Y.-L., and Ryu, S. C., 2019, "Performance Evaluation of Optically Sensorized Tendons for Articulate Surgical Instruments," J. Med. Device., **13**(4), pp. 044504–044511.
[63] Moreira, P., Kuil, leanne, Dias, P., Borra, R., Misra, S., Jun, C., Lim, S., Wolinsky, J.-P., Garzon, T., Petrisor, D., Cleary, K., Stoianovici, D., Matheson, E., Secoli, R., Burrows,

C., Leibinger, A., y Baena, F., Morgan, N. B., Honarvar, M., Konh, B., Podder, T. K., Dicker, A. P., Yu, Y., Hutapea, P., Uchil, J., Fernandes, F. M. B., Mahesh, K. K., Mohd Jani, J., Leary, M., Subic, A., Gibson, M. A., Roesthuis, R. J., Kemp, M., van den Dobbelsteen, J. J., Misra, S., Abayazid, M., Kemp, M., Misra, S., Liang, W., Huang, Y., Xu, Y., Lee, R. K., Yariv, A., Robert J. Webster, I. I. I., Kim, J. S., Cowan, N. J., Chirikjian, G. S., Okamura, A. M., Hauser, K., Alterovitz, R., Chentanez, N., Okamura, A. M., Goldberg, K., Glozman, D., Shoham, M., Patil, S., Burgner, J., Webster, R. J., Alterovitz, R., Karthikeyan, R., Sigmund, K., Park, Y.-L., Ryu, S. C., Quek, Z. F., Koh, J.-S., Renaud, P., Black, R. J., Moslehi, B., Daniel, B. L., Cho, K.-J., Cutkosky, M. R., Kutzer, M. D. M., Segreti, S. M., Brown, C. Y., Armand, M., Taylor, R. H., Mears, S. C., Haga, Y., Muyari, Y., Goto, S., Matsunaga, T., Esashi, M., Varnamkhasti, Z. K., Konh, B., York, P. A., Swaney, P. J., Gilbert, H. B., Webster, R. J., Chitalia, Y., Deaton, N. J., Jeong, S., Rahman, N., Desai, J. P., Gerboni, G., Greer, J. D., Laeseke, P. F., Hwang, G. L., Okamura, A. M., Su, H., Li, G., Rucker, D. C., Webster III, R. J., Fischer, G. S., van de Berg, N. J., Dankelman, J., van den Dobbelsteen, J. J., Ryu, S. C., Renaud, P., Black, R. J., Daniel, B. L., Cutkosky, M. R., Ayvali, E., Liang, C.-P., Ho, M., Chen, Y., Desai, J. P., Haddadi, A., Goksel, O., Salcudean, S. E., Hashtrudi-Zaad, K., Rossa, C., Tavakoli, M., Alfalahi, H., Renda, F., Stefanini, C., Meltsner, M. A., Ferrier, N. J., Thomadsen, B. R., Misra, S., Reed, K. B., Schafer, B. W., Ramesh, K. T., Okamura, A. M., Abolhassani, N., Patel, R., Moallem, M., Sears, P., Dupont, P., Webster, R. J., Romano, J. M., Cowan, N. J., Swaney, P. J., Burgner, J., Gilbert, H. B., Webster, R. J., Wedlick, T. R., Okamura, A. M., Reed, K. B., Majewicz, A., Kallem, V., Alterovitz, R., Goldberg, K., Cowan, N. J., Okamura, A. M., Okazawa, S., Ebrahimi, R., Chuang, J., Salcudean, S. E., Rohling, R., Gilbert, H. B., Rucker, D. C., Webster III, R. J., Cowan, N. J., Goldberg, K., Chirikjian, G. S., Fichtinger, G., Alterovitz, R., Reed, K. B., Kallem, V., Park, W., Misra, S., Okamura, A. M., Moreira, P., van de Steeg, G., Krabben, T., Zandman, J., Hekman, E. E. G., van der Heijden, F., Borra, R., Misra, S., Tsumura, R., Takishita, Y., Iwata, H., Carriere, J., Khadem, M., Rossa, C., Usmani, N., Sloboda, R., Tavakoli, M., Yang, F., Babaiasl, M., Swensen, J. P., van de Berg, N. J., van Gerwen, D. J., Dankelman, J., and van den Dobbelsteen, J. J., 2019, "Concentric Tube Robots for Minimally Invasive Surgery: Current Applications and Future Opportunities," J. Med. Robot. Res., **04**(4), pp. 1–11.

[64] Chitalia, Y., Jeong, S., Deaton, N., Chern, J. J., and Desai, J. P., 2020, "Design and Kinematics Analysis of a Robotic Pediatric Neuroendoscope Tool Body," IEEE/ASME Trans. Mechatronics, **25**(2), pp. 985–995.

[65] de Vries, M., Sikorski, J., Misra, S., and van den Dobbelsteen, J. J., 2021, "Axially Rigid Steerable Needle with Compliant Active Tip Control," PLoS One, **16**(12), pp. 1–18.

[66] Moreira, P., Boskma, K. J., and Misra, S., 2017, "Towards MRI-Guided Flexible Needle Steering Using Fiber Bragg Grating-Based Tip Tracking," *2017 IEEE International Conference on Robotics and Automation (ICRA)*, pp. 4849–4854.

[67] Shahriari, N., Georgiadis, J. R., Oudkerk, M., and Misra, S., 2019, "Hybrid Control Algorithm for Flexible Needle Steering: Demonstration in Phantom and Human Cadaver," PLoS One, **13**(12), pp. 1–15.

[68] Adebar, T. K., Fletcher, A. E., and Okamura, A. M., 2014, "3-D Ultrasound-Guided Robotic Needle Steering in Biological Tissue," IEEE Trans. Biomed. Eng., **61**(12), pp. 2899–2910.

[69] Padasdao, B., Varnamkhasti, Z. K., and Konh, B., 2020, "3D Steerable Biopsy Needle with a Motorized Manipulation System and Ultrasound Tracking to Navigate inside Tissue," J. Med. Robot. Res., **5**(03n04), p. 2150003.
[70] Padasdao, B., and Konh, B., 2020, "Shape Memory Alloy Actuators in an Active Needle - Modeling, Precise Assembly and Performance Evaluation," J. Manuf. Sci. Eng., **143**, pp. 1–25.
[71] DiMaio, S. P., and Salcudean, S. E., 2003, "Needle Steering and Model-Based Trajectory Planning," *Medical Image Computing Computer-Assisted Intervention*, pp. 33–40.
[72] Glozman, D., and Shoham, M., 2007, "Image-Guided Robotic Flexible Needle Steering," IEEE Trans. Robot., **23**(3), pp. 459–467.
[73] Hauser, K., Alterovitz, R., Chentanez, N., Okamura, A., and Goldberg, K., 2009, "Feedback Control for Steering Needles Through 3D Deformable Tissue Using Helical Paths.," Robot. Sci. Syst., **V**, p. 37.
[74] Lagoudas, D. C., 2008, *Shape Memory Alloys: Modeling and Engineering Applications*, Springer, New York.
[75] Elahinia, M. H., 2016, *Shape Memory Alloy Actuators: Design, Fabrication, and Experimental Evaluation*, Wiley.
[76] Mohd Jani, J., Leary, M., Subic, A., and Gibson, M. A., 2014, "A Review of Shape Memory Alloy Research, Applications and Opportunities," Mater. Des., **56**(April), pp. 1078–1113.
[77] Case, L., 2004, *Shape Memory Alloy Shape Training Tutorial*, Transformation.
[78] L. Lecce and A. Concilio, 2015, *Shape Memory Alloy Engineering*, Elsevier Science.
[79] "Memry Corporation" [Online]. Available: https://www.memry.com/#nitinol.
[80] Uchil, J., Fernandes, F. M. B., and Mahesh, K. K., 2007, "X-Ray Diffraction Study of the Phase Transformations in NiTi Shape Memory Alloy," Mater. Charact., **58**(3), pp. 243–248.
[81] Migliavacca, L. P. and F., 2011, "Biomedical Applications of Shape Memory Alloys," J. Met., pp. 1–15.
[82] Morgan, N. B., 2004, "Medical Shape Memory Alloy Applications—the Market and Its Products," Mater. Sci. Eng. A, **378**(1–2), pp. 16–23.
[83] Zheng, Y., Wu, J., Chen, S., Liu, Y., and Zhang, G., 2018, "Predicting Pubic Arch Interference in Permanent Prostate Brachytherapy Based on the Specific Parameters Derived from Nuclear Magnetic Resonance Imaging," J. Contemp. Brachytherapy, **10**(5), pp. 405–410.
[84] Zhang, S.-J., Qian, H.-N., Zhao, Y., Sun, K., Wang, H.-Q., Liang, G.-Q., Li, F.-H., and Li, Z., 2013, "Relationship between Age and Prostate Size.," Asian J. Androl., **15**(1), pp. 116–120.
[85] Eastwood, K. W., Francis, P., Azimian, H., Swarup, A., Looi, T., Drake, J. M., and Naguib, H. E., 2018, "Design of a Contact-Aided Compliant Notched-Tube Joint for Surgical Manipulation in Confined Workspaces," J. Mech. Robot., **10**(1), pp. 1–12.
[86] Datla, N. V., Konh, B., Honarvar, M., Podder, T. K., Dicker, A. P., Yu, Y., and Hutapea, P., 2014, "A Model to Predict Deflection of Bevel-Tipped Active Needle Advancing in Soft Tissue," Med. Eng. Phys., **36**(3), pp. 285–293.
[87] Konh, B., Padasdao, B., Batsaikhan, Z., and Ko, S. Y., 2021, "Integrating Robot-assisted Ultrasound Tracking and 3D Needle Shape Prediction for Real-time Tracking of the Needle Tip in Needle Steering Procedures," Int. J. Med. Robot. Comput. Assist. Surg.

[88] S. Natarajan, A. Priester, D. Margolis, J. Huang, A., and Marks, L., 2022, "Prostate MRI and Ultrasound With Pathology and Coordinates of Tracked Biopsy (Prostate-MRI-US-Biopsy)," Cancer Imaging Arch.

[89] Sonn, G. A., Natarajan, S., Margolis, D. J. A., MacAiran, M., Lieu, P., Huang, J., Dorey, F. J., and Marks, L. S., 2013, "Targeted Biopsy in the Detection of Prostate Cancer Using an Office Based Magnetic Resonance Ultrasound Fusion Device.," J. Urol., **189**(1), pp. 86–91.

[90] Clark, K., Vendt, B., Smith, K., Freymann, J., Kirby, J., Koppel, P., Moore, S., Phillips, S., Maffitt, D., Pringle, M., Tarbox, L., and Prior, F., 2013, "The Cancer Imaging Archive (TCIA): Maintaining and Operating a Public Information Repository," J. Digit. Imaging, **26**(6), pp. 1045–1057.

[91] Chitalia, Y., Jeong, S., Yamamoto, K. K., Chern, J. J., and Desai, J. P., 2020, "Modeling and Control of a 2-DoF Meso-Scale Continuum Robotic Tool for Pediatric Neurosurgery," IEEE Trans. Robot., pp. 1–12.

[92] Ryu, S. C., Quek, Z. F., Renaud, P., Black, R. J., Daniel, B. L., and Cutkosky, M. R., 2012, "An Optical Actuation System and Curvature Sensor for a MR-Compatible Active Needle," *IEEE International Conference on Robotics and Automation*, (Saint Paul, MN, May), pp. 1589–1594.